

Magnetic-field-induced topological phase transition in Fe-doped (Bi,Sb)₂Se₃ heterostructures

Y. Satake^{1,2}, J. Shiogai^{1,*}, G. P. Mazur², S. Kimura¹, S. Awaji¹, K. Fujiwara¹, T. Nojima¹,
K. Nomura^{1,3}, S. Souma^{3,4}, T. Sato^{3,4,5}, T. Dietl^{2,4}, and A. Tsukazaki^{1,3}

¹*Institute for Materials Research, Tohoku University, Sendai 980-8577, Japan*

²*International Research Centre MagTop, Institute of Physics, Polish Academy of Sciences,
Aleja Lotnikow 32/46, PL-02668 Warsaw, Poland*

³*Center for Spintronics Research Network (CSRN), Tohoku University, Sendai 980-8577,
Japan*

⁴*WPI-Advanced Institute for Materials Research, Tohoku University, Sendai 980-8577,
Japan*

⁵*Department of Physics, Tohoku University, Sendai 980-8578, Japan*

*Author to whom correspondence should be addressed.

Electronic mail: junichi.shiogai@imr.tohoku.ac.jp

Abstract

Three-dimensional topological insulators (3D-TIs) possess a specific topological order of electronic bands, resulting in gapless surface states via bulk-edge correspondence. Exotic phenomena have been realized in ferromagnetic TIs, such as the quantum anomalous Hall (QAH) effect with a chiral edge conduction and a quantized value of the Hall resistance R_{yx} . Here, we report on the emergence of distinct topological phases in paramagnetic Fe-doped $(\text{Bi,Sb})_2\text{Se}_3$ heterostructures with varying structure architecture, doping, and magnetic and electric fields. Starting from a 3D-TI, a two-dimensional insulator appears at layer thicknesses below a critical value, which turns into an Anderson insulator for Fe concentrations sufficiently large to produce localization by magnetic disorder. With applying a magnetic field, a topological transition from the Anderson insulator to the QAH state occurs, which is driven by the formation of an exchange gap owing to a giant Zeeman splitting and reduced magnetic disorder. Topological phase diagram of $(\text{Bi,Sb})_2\text{Se}_3$ allows exploration of intricate interplay of topological protection, magnetic disorder, and exchange splitting.

I. Introduction

Three-dimensional topological insulators (3D-TI) are a class of matter that composed of gapless surface states and insulating bulk [1-3]. In such material systems, various types of topological phase transitions (TPTs) are expected to appear as a result of structural modifications and application of external fields [4-13]. For instance, an exchange gap formation in the surface states engenders a TPT, which leads to the quantum anomalous Hall (QAH) phase, i.e., to the Chern insulator. In this phase, similarly to the conventional quantum Hall effect (QHE), charge transport proceeds via a dissipationless chiral edge channel while the origin is completely different [14-16]; the QAHE is driven by the formation of an exchange gap and the QHE by Landau level splitting. To materialize the QAH phase in TIs, the surface electronic states should be modified by the exchange gap owing to some mechanisms (1) coupling between surface state and ferromagnetically aligned spins of transition metal impurities [15-17] or aligned spins by external magnetic field in the antiferromagnetic topological insulator [18,19], (2) proximity coupling effect with adjacent magnetic moment [20-22], or (3) band crossing driven by a Zeeman splitting [17,23]. To date, experimental observations of the QAH effect have been accomplished for Cr-doped or V-doped $(\text{Bi,Sb})_2\text{Te}_3$ (BST) 3D-TI films, where a perpendicular spontaneous magnetization develops below the Curie temperature

(type (1)) [15,16,24-28], and for a proximitized $(\text{Bi,Sb})_2\text{Te}_3$ /ferromagnetic insulator heterostructure (type (2)) [29]. In contrast, type (3) of QAH has not been observed in paramagnetic $(\text{Bi,Sb})_2\text{Se}_3$ -based TIs, whereas the quantization of the Hall resistance is accomplished by the application of a magnetic field to a 4 quintuple layer of Cr-doped $(\text{Bi,Sb})_2\text{Te}_3$ [30], Ti-doped $(\text{Bi,In})_3\text{Te}_2$ [31], and MnBi_2Te_4 [18,19].

As another TPT, the surface state can be gapped when the 3D-TI film is sufficiently thin to activate hybridization of states from the opposite surfaces [1,2]. Thin films of Bi_2Se_3 -type 3D-TIs are known to be 2D trivial insulators [4,32-34] when the hybridization is sufficiently strong, as presented in Fig. 1(a). Considering this trivial electronic band as an initial state, the giant Zeeman splitting generated by an external magnetic field produces a specific band crossing (Fig. 1(b)) with formation of an exchange gap (Fig. 1(c)) [17,23] at this crossing point, equivalent to that driven by type (1) and (2) in coupling with ferromagnetic systems, inducing a conceptually different type (3) of QAH. To illustrate the topological phase transition from the hybridized insulator to the QAH phase driven by the Zeeman splitting, we have calculated the band structure using a 3D-TI slab geometry. Figures 1(d)-1(f) demonstrate the band modification of 3D-TI by the inter-surface hybridization and the Zeeman effect. When Δ_{hy} is larger than Δ_{Zeeman} , the hybridized insulator is stabilized without surface gapless states (Fig. 1(d)).

The Δ_{Zeeman} exceeding Δ_{hy} forms a non-trivial exchange gap with one-dimensional chiral-edge channel as shown in Figs. 1(e) and 1(f), with gap size proportional to the magnetic field. In Fig. 1(f), red (blue) thick curve shows the chiral edge mode at one (the other) edge.

With a minor contribution of the ordinary Hall effect under magnetic field owing to Fermi energy (E_F) locating in the gap, the magnetic-field-induced anomalous Hall effect plays a critical role for the quantization of the Hall conductivity. This study demonstrates the presence of TPTs between 3D-TI, a two-dimensional (2D) insulator, and QAH phases in paramagnetic Fe-doped Bi_2Se_3 -based heterostructures by controlling Fe doping and layer thickness and by application of external magnetic and electric fields.

The tetradymite compound Bi_2Se_3 is a representative 3D-TI, in which a large bulk band gap (approximately 300 meV) hosts gapless surface states [35]. Using angle-resolved photoemission spectroscopy (ARPES) of surface states, 50 meV gap formation was detected in paramagnetic Fe-doped bulk Bi_2Se_3 ; it was assigned to breakage of the time-reversal symmetry by exchange interactions [36]. Effects of magnetic impurities upon topological surface states were also studied by *in-situ* deposition of Fe atoms [37-39]. It was found that Fe acts as donor [37,38] if deposited at room temperature but as an acceptor if deposited at 8 K [38]. A question on whether the presence of a Fe surface layer

opens a gap or not in the topological states was also examined experimentally and theoretically [37-39].

According to one theoretical proposal, Fe-doped Bi_2Se_3 -based heterostructures are a preferred platform for observing the emergence of QAH phase [17]. Nevertheless, no QAH effect has yet been observed in magnetically doped Bi_2Se_3 -based films, probably because of the absence or weakness of the ferromagnetic ordering, and associated difficulties in tuning of the E_F into a correspondingly small exchange gap [40]. In contrast, a TPT from the TI to the 2D-insulator by film thickness reduction was demonstrated for Bi_2Se_3 films using ARPES and electrical measurements [4,31-33]. Depending on the experimental method used, the critical thickness for the transition has been reported as 5 [4] or 10 nm [41] in Bi_2Se_3 . For other 3D-TIs such as Bi_2Te_3 , $(\text{Bi,Sb})_2\text{Te}_3$ (BST) and magnetically doped BST films, variations in the strength of the spin-orbit interaction are thought to account for critical thickness changes from 1 to 13 nm [12,42].

II. EXPERIMENTAL DETIALS

Employing molecular-beam epitaxy (MBE) and a 3-nm-thick n -type Bi_2Se_3 buffer layer on a semi-insulating Fe-doped InP (111) substrate, we have grown $\text{Fe}_x(\text{Bi}_{1-y}\text{Sb}_y)_{2-x}\text{Se}_3$ films of thickness d ranging from 8 to 30 nm (see Supplementary section 1

[43]),. The control parameters are the Sb composition and the gate bias voltage for changing the E_F position [44,45], whereas the Fe concentration and the external magnetic field serve for tuning magnetic disorder and band splitting state. Because Fe doping up to at least $x = 0.1$ (nominal composition controlled by the beam flux ratio) produces rather minor changes in R_{xx} and $|R_{yx}|$ magnitudes (see Supplementary section 2 [43]), we infer that Fe ions are isoelectronic impurities occupying Bi or Sb sites, and assume the same Fe^{3+} charge configuration with bulk Fe-doped Bi_2Se_3 [36] that typically corresponds to the high spin $S = 5/2$. However, Fe acts not only as a magnetic impurity, but also as an isoelectronic dopant, in a manner similar to Sb, which affects the carrier concentration owing to band shifts with respect to defect formation levels. Moreover, thickness d plays a crucially important role in the control of both (i) hybridization between surface and interfacial topological states and (ii) the width of the depletion layer in the p - n junction that forms at the interface to the n -type Bi_2Se_3 buffer layer.

III. RESULT AND DISCUSSION

A. Angle-resolved photoemission spectroscopy (ARPES) and magnetic properties

We have characterized the electronic structure of a 30-nm-thick $\text{Fe}_{0.05}(\text{Bi}_{0.34}\text{Sb}_{0.66})_{1.95}\text{Se}_3/\text{Bi}_2\text{Se}_3$ heterostructure at 40 K using ARPES. As presented in Fig.

1(g), the topological surface states and the bulk valence band are resolved clearly at the Γ point, indicating that this thick Fe-doped $(\text{Bi,Sb})_2\text{Se}_3$ layer preserves key features of 3D-TIs and does not engender a substantial Fermi level shift. Linear dispersion of the surface band is more readily apparent when moving the Fermi level up in energy by an aging process that increases the surface electron concentration (see Fig. S3 [43]). Contrary to an earlier report on ARPES at 10 K of bulk Fe-doped Bi_2Se_3 samples with Fe concentration $x = 0.12$ and 0.16 , which was considered as a consequence of ferromagnetic ordering [36], no sizable gap in the surface states is resolved in the case of our MBE-grown layer with $x = 0.05$; this indicates the absence of a long range magnetic order at Fe concentration of interest here.

The ARPES data are consistent with the magnetotransport studies: neither hysteretic nor saturation behavior has been observed in our Hall effect measurements, indicating that Fe ions remain in a paramagnetic phase down to 2 K for $x = 0.05$. This is in agreement with previous direct measurements of magnetization $M(T,H)$ down to 2 K and up to $\mu_0 H = 5$ T on bulk samples that showed paramagnetic behavior below $x = 0.16$ [36]. Some hysteresis superimposed on the paramagnetic signal $M(H)$ were detected for $x \geq 0.16$ at 2 K [36]. The absence of ferromagnetism at low Fe concentrations is consistent with our direct magnetization measurements employing superconducting quantum

interference device (SQUID), which do not show any hysteresis. However, a quantitative evaluation of the epilayer paramagnetic signal from our SQUID and electron paramagnetic resonance studies has been hampered by a small thickness of the epilayers and a large magnetic contribution of the Fe-doped InP substrate. The absence of ferromagnetism in the Fe-doped Bi_2Se_3 is also consistent with *ab initio* studies [46,47].

B. Magnetotransport properties

The values of the 2D resistivity tensor components, *i.e.*, the sheet resistance R_{xx} and the Hall resistance R_{yx} , have been measured in the Hall-bar geometry and using a standard lock-in technique [43]. Figure 1(h) presents a contour plot of R_{xx} values for $\text{Fe}_{0.05}(\text{Bi}_{0.34}\text{Sb}_{0.66})_{1.95}\text{Se}_3/\text{Bi}_2\text{Se}_3$ films in $B = 0$ as a function of layer thickness d and temperature T (see Supplementary Fig. S4(a) for detailed dataset [43]). One phenomenological criterion describing the critical point of the localization transition in the 2D case is the sheet resistance value of $h/e^2 \cong 25.8 \text{ k}\Omega$ [48,49]. The boundary is pronounced as a white color region in Fig. 1(h). As shown there, $R_{xx}(T)$ determined for the 30-nm-thick film shows lower values than that of h/e^2 , in addition to weak temperature dependence, implying that this sample is the 3D-TI phase (Fig. 1(g)). With decreasing d at fixed Fe and Sb concentrations ($x = 0.05$ and $y = 0.66$), $R_{xx}(T)$ reaches the critical value of h/e^2 at thickness of $d = 14 \text{ nm}$, below which dependence $R_{xx}(T)$ exhibits insulating

behavior and R_{xx} magnitudes exceed $1 \text{ M}\Omega$ at the lowest temperature of 2 K (deep-red region in Fig. 1(h)). Such highly insulating features at $d < 14 \text{ nm}$ can be ascribed either to the trivial Anderson insulator [50,51] or to the quantum spin Hall insulator [51,52], if the formation of edge states would accompany hybridization of surface states. However, edge conductance would hardly dominate the charge transport in the present Hall-bar geometry with the channels longer than the expected protection length of helical topological channels. The phase coherence length estimated by weak antilocalization analysis of the Bi_2Se_3 thin films is about 200 nm [45], which is well below the channel length. In principle, ARPES is an effective way to tell the topological phase. However, the high resistance and the corresponding charging effect made it difficult to assess the electronic structure of our thinnest samples. Nevertheless, the critical thickness we found for this 2D-insulator is rather thick compared to the values (5–10 nm) reported for non-magnetic Bi_2Se_3 films [4,41]. This point can be explained by the empirical fact (see Supplementary Section 5 [43]) that the substitution of heavier Bi or Sb by lighter Fe reduces the spin-orbit interaction strength, which might increase the critical thickness. Furthermore, the presence of the n -type Bi_2Se_3 buffer layer depletes the p -type $\text{Fe}_{0.05}(\text{Bi}_{0.34}\text{Sb}_{0.66})_{1.95}\text{Se}_3$ layer [45], making the effective thickness less than the nominal value.

More importantly, in our paramagnetic samples, spin disorder scattering by Fe impurities can be effective for expanding the Anderson insulator range with regard to the thickness and temperature of $\text{Fe}_x(\text{Bi}_{1-y}\text{Sb}_y)_{2-x}\text{Se}_3$ films (Fig. 1(h)), making it wider compared to Bi_2Se_3 . Temperature dependence of resistivity for samples with $d = 14$ nm and various x are presented in Fig. S2 [43]. The data show clearly a transition from the weakly localized regime to the strongly localized regime, characterized by a sharp increase of resistivity on lowering temperature, which appears at $x > 0.04$. As expected in the absence of Landau quantization and in the 2D case [53], this transition has a cross-over character, so that it does not obey scaling equations. As presented in Fig. 1(i), the magnitude of magnetoresistance defined as $\text{MR} = [R_{xx}(B) - R_{xx}(0)]/R_{xx}(0)$ exceeds -80% in 9 T and at 2 K in the vicinity of the localization transition. The ordering of Fe spins in the magnetic field reduces magnetic disorder and enhances the spin splitting of electronic states. Consequently, a QAH phase would appear in the thickness region toward type (3) by the application of the magnetic field as schematically shown in Fig. 1(c) and 1(f). In accordance with the expectation that reduction of magnetic disorder occurs for any field direction, we find negative MR to be also present for the in-plane magnetic field (Supplementary Fig. S6 [43]).

Figure 2 presents a dependence of Hall resistance R_{yx} on the Sb concentration y

at $T = 2$ K and $B = 9$ T for $\text{Fe}_{0.05}(\text{Bi}_{1-y}\text{Sb}_y)_{1.95}\text{Se}_3/\text{Bi}_2\text{Se}_3$ with $d \cong 14$ nm (red circles). This dependence is strikingly different compared to the case of non-magnetic $(\text{Bi}_{1-y}\text{Sb}_y)_2\text{Se}_3/\text{Bi}_2\text{Se}_3$ films with $d = 14\text{--}20$ nm (black squares) [44]. The representative raw data of $R_{yx}(B)$ for Fe-doped samples are shown in the inset. For non-magnetic $(\text{Bi}_{1-y}\text{Sb}_y)_2\text{Se}_3/\text{Bi}_2\text{Se}_3$, the sign reversal of R_{yx} reflects the conversion of the carrier type and therefore the tuning of E_F across the charge neutrality point (CNP), which appears at $y \cong 0.7$. In contrast, the R_{yx} in the Fe-doped films persists positive value in $y > 0.5$ indicates that the positive contribution of magnetic-field-induced anomalous Hall resistance is much larger than the negative contribution of ordinary Hall component; empirically $R_{yx} = R_0B + R_A M_z$ where R_0 is the ordinary Hall coefficient, B magnetic field, R_A the anomalous Hall coefficient, and M_z out-of-plane component of magnetization. By application of a perpendicular B , B -induced M_z is dominantly contribute to the R_{yx} with negligibly small ordinary component. Moreover, R_{yx} is enhanced greatly with a peak at $y \cong 0.67$, close to the CNP in non-magnetic films. The behavior of R_{yx} as a function of y , together with a large magnitude of R_{yx} at the CNP, demonstrate that R_{yx} is dominated by the intrinsic anomalous Hall effect, as its amplitude is expected to be dependent on the E_F position while its sign is determined by magnetization direction and exchange coupling [17,19,54]. In fact, the tangent of Hall angle R_{yx}/R_{xx} approaches unity at values greater

than $d = 14$ nm (see Supplementary Fig. S4(f) [43]) indicating that the condition for the Landau quantization of the density of states, $R_0 B / R_{xx} > 1$, is not met. It should be noted that such a large R_{yx} at $d = 14$ nm is observed also in the insulator region (Fig. 1(h)), where negative MR exists (Fig. 1(i)).

Together with revealing enhanced values of $R_{yx}(B)$, transition behavior is found in $R_{xx}(T)$ in elevated fields up to 24 T, as depicted in Fig. 3(a). The field-induced insulator-metal transition becomes apparent below 50 K. For $B > 12$ T, the metallicity increases concomitantly with increasing B down to temperatures as low as 1.6 K. The criterion in $B = 9$ T for the sign change of dR_{xx}/dT being close to $0.5 \hbar/e^2$. This value for the MIT, compared to $1 \hbar/e^2$ for MIT driven by structural modifications (cf. Fig. 1(h)), indicates one other type of the TPT. We attributed this field-induced metallization to a TPT from the 2D-insulator to a QAH phase. The insulator at $B = 0$ with hybridization gap Δ_{hy} (Fig. 1(a) and 1(d)) turns to be a state with inverted bands by Zeeman splitting Δ_{Zeeman} when $\Delta_{Zeeman} > \Delta_{hy}$. With the assistance of spin-orbit coupling, a gap is formed at the crossings of surface bands hosting carriers with opposite spin orientations [17,30], as depicted in Fig. 1(c) and 1(f). Furthermore, at $\Delta_{Zeeman} > \Delta_{hy}$, gapless disorder-protected chiral channels are formed, in a full analogy to the theoretical proposal for the QAH effect [17].

Having observed the signature of this new TPT, we study $R_{xx}(B)$ and $R_{yx}(B)$ at T

= 1.6 K employing a field-effect transistor (FET) device for precise tuning of E_F . The FET layout is depicted in the inset shown with Fig. 3(b) (see also Supplementary Materials [43]) – it consists of a 1-nm-thick Bi_2Se_3 /18.5-nm-thick $\text{Fe}_{0.05}(\text{Bi}_{0.33}\text{Sb}_{0.67})_{1.95}\text{Se}_3$ /3-nm-thick Bi_2Se_3 trilayer structure. As depicted in Fig. 3(b), by sweeping magnetic field up to 15 T under $V_G = -60$ V, the large R_{xx} value of $3.92 h/e^2$ in $B = 0$ (black line) decreases monotonically to $0.2 h/e^2$ whereas R_{yx} (red line) increases, reaching $0.975 h/e^2$, i.e., almost the value expected for the ideal QAH phase, h/e^2 . Consequently, the magnetic-field-induced transition from the 2D-insulator to the QAH phase can be observed clearly at the high temperature of $T = 1.6$ K, at which the quantization accuracy of the R_{yx} value is comparable to that reported for Cr modulation doped $(\text{Bi,Sb})_2\text{Te}_3$ heterostructures [15,55] and higher than that for Cr-doped or V-doped $(\text{Bi,Sb})_2\text{Te}_3$ thin films [8,24-28]. Note that this quantization is hardly considered to be QHE due to insulating initial state at $B = 0$ with a negligible ordinary Hall effect. The electrostatic tuning of the E_F position with respect to the gap around the CNP promotes other TPTs as presented in conductivity tensor in Supplementary Fig. S10 [43].

The nature of relevant phases is assessed by examining the renormalization group flow of the conductivity tensor components [$\sigma_{xx} = R_{xx}/(R_{xx}^2 + R_{yx}^2)$, $\sigma_{xy} = R_{yx}/(R_{xx}^2 + R_{yx}^2)$] as a function of temperature [8,25,56]. Figures 4(a) and 4(b) show $\sigma_{xx}(T)$ and

$\sigma_{xy}(T)$ for various B at $V_G = -60$ V. As T decreases, all $\sigma_{xx}(T)$ values decrease, irrespective of B . However, $\sigma_{xy}(T)$ goes to e^2/h and to zero, respectively, in high and low fields, with a crossover point of about $0.5 e^2/h$. These data are shown in the $[\sigma_{xy}(B), \sigma_{xx}(B)]$ plane in Fig. 4(c). By lowering T from 15 K (open symbols) to 1.6 K (close symbols) under various magnetic fields, the data converge to either $(\sigma_{xx}, \sigma_{xy}) = (0, 0)$ for the insulator or $(0, e^2/h)$ for QAH phase. The finding of a converging point in our Fe-doped $(\text{Bi,Sb})_2\text{Se}_3$ samples clearly evidences the presence of a phase transition driven by the magnetic field, with the critical field of 7–8 T corresponding to the point at which Δ_{Zeeman} becomes comparable to Δ_{hy} . Moreover, as shown in Supplementary Fig. S10 [43], the transition driven by an electric field in fixed magnetic fields of 9 and 12 T is visible. Given the experimental observation of the TPT in the accessible magnetic field, the large g -factor of the surface state should be taken into consideration to estimate Δ_{Zeeman} , as discussed in Supplementary Section 9 [43]. The Zeeman splitting (g -factor of $\text{Bi}_2\text{Se}_3 \sim 18\text{-}50$ [57,58]) can be enhanced considerably over the band value $g^* \mu_B B$ through the sp - d exchange interaction between itinerant carriers and localized magnetic moments, as observed in various dilute magnetic semiconductors, primarily doped with Mn but also with Fe^{3+} ions [59]. By applying g -factor engineering, the TPT might be shifted to much weaker magnetic fields and higher temperatures. The renormalization group flow for type (3) in paramagnetic $(\text{Bi,Sb})_2\text{Se}_3$

film (Fig. 1(c) and 1(f)) can be understood in terms of universal QAH phenomenon as previously discussed in type (1) in ferromagnetic $(\text{Bi,Sb})_2\text{Te}_3$ films [8,25,56].

IV. Conclusion

We have performed comprehensive study of topological phase transitions based on Fe-doped $(\text{Bi,Sb})_2\text{Se}_3$ thin films, which are driven by structural modification, doping, and external magnetic and electric fields. We found that topological phase transition occurs from 3D-TI to 2D-insulator by Fe doping owing to localization by magnetic disorder. The 2D-insulator is turned to QAH state by external magnetic field owing to a large Zeeman splitting and suppression of the magnetic disorder. Demonstration of the magnetic-field-induced TPT toward the QAH state in Bi_2Se_3 -based 3D-TI sheds light on new perspectives of the QAH physics and expands it to a broader class of paramagnetic TI materials with properties that can be controlled by g -factor engineering.

Acknowledgments

This work was partly supported by CREST (No. JPMJCR18T1 and JPMJCR18T2), the Japan Science and Technology Agency, a Grant-in-Aid for Scientific Research on Innovative Areas (No. JP15H05853), and a Grant-in-Aid for Young Scientists (A) (No. 16H05981). Y.S. was supported by Kato Foundation for Promotion of Science (Grant No. KS-2914). The work in Poland was funded by the Foundation for Polish Science through the IRA Programme financed by EU within SG OP Programme. We thank NEOARK Corporation for the use of photolithography equipment for device fabrication.

References

1. M. Z. Hasan and C. L. Kane, Colloquium: Topological insulators, *Rev. Mod. Phys.* **82**, 3045 (2010).
2. X. L. Qi and S. C. Zhang, Topological insulators and superconductors, *Rev. Mod. Phys.* **83**, 1057 (2011).
3. Y. Ando, Topological insulator Materials, *J. Phys. Soc. Jpn.* **82**, 102001 (2013).
4. Y. Zhang, K. He, C. Z. Chang, C. L. Song, L. L. Wang, X. Chen, J. F. Jia, Z. Fang, X. Dai, W. Y. Shan *et al.*, Crossover of the three-dimensional topological insulator Bi_2Se_3 to the two-dimensional limit, *Nat. Phys.* **6**, 584 (2010).
5. T. Sato, K. Segawa, K. Kosaka, S. Souma, K. Nakayama, K. Eto, T. Minami, and Y. Ando, Unexpected mass acquisition of Dirac fermions at the quantum phase transition of a topological insulator, *Nat. Phys.* **7**, 840 (2011).
6. M. Brahlek, N. Bansal, N. Koirala, S. Y. Xu, M. Neupane, C. Liu, M. Z. Hasan, and S. Oh, Topological-metal to band-insulator transition in $(\text{Bi}_{1-x}\text{In}_x)_2\text{Se}_3$ thin films, *Phys. Rev. Lett.* **109**, 186403 (2012).
7. J. Zhang, C. Z. Chang, P. Tang, Z. Zhang, X. Feng, K. Li, L. Wang, X. Chen, C. Liu, W. Duan *et al.*, Topology-driven magnetic quantum phase transition in

- topological insulators, *Science* **339**, 1582 (2013).
8. X. Kou, L. Pan, J. Wang, Y. Fan, E. S. Choi, W. L. Lee, T. Nie, K. Murata, Q. Shao, S. C. Zhang, and K. L. Wang, Metal-to-insulator switching in quantum anomalous Hall states, *Nat. Commun.* **6**, 8474 (2015).
 9. Y. Feng, X. Feng, Y. Ou, J. Wang, C. Liu, L. Zhang, D. Zhao, G. Jiang, S. C. Zhang, K. He *et al.*, Observation of the zero Hall plateau in a quantum anomalous Hall insulator, *Phys. Rev. Lett.* **115**, 126801 (2015).
 10. C. Z. Chang, W. Zhao, J. Li, J. K. Jain, C. Liu, J. S. Moodera, and M. H. W. Chan, Observation of the quantum anomalous Hall insulator to Anderson insulator quantum phase transition and its scaling behavior, *Phys. Rev. Lett.* **117**, 126802 (2016).
 11. M. Mogi, M. Kawamura, R. Yoshimi, A. Tsukazaki, Y. Kozuka, N. Shirakawa, K. S. Takahashi, M. Kawasaki, and Y. Tokura, A magnetic heterostructure of topological insulators as a candidate for an axion insulator, *Nat. Mater.* **16**, 516 (2017).
 12. M. Kawamura, M. Mogi, R. Yoshimi, A. Tsukazaki, Y. Kozuka, K. S. Takahashi, M. Kawasaki, and Y. Tokura, Topological quantum phase transition in magnetic

- topological insulator upon magnetization rotation, *Phys. Rev. B* **98**, 140404(R) (2018).
13. D. Xiao, J. Jiang, J. H. Shin, W. Wang, F. Wang, Y. F. Zhao, C. Liu, W. Wu, M. H. W. Chan, N. Samarth, and C. Z. Chang, Realization of the axion insulator state in quantum anomalous Hall sandwich heterostructures, *Phys. Rev. Lett.* **120**, 056801 (2018).
 14. S. Oh, The complete quantum Hall trio, *Science* **340**, 153 (2013).
 15. Y. Tokura, K. Yasuda, and A. Tsukazaki, Magnetic topological insulators, *Nat. Rev. Phys.* **1**, 126 (2019).
 16. C. Z. Chang, and M. Li, Quantum anomalous Hall effect in time-reversal-symmetry breaking topological insulators, *J. Phys. Condens. Matter.* **28**, 123002 (2016).
 17. R. Yu, W. Zhang, H. J. Zhang, S. C. Zhang, X. Dai, and Z. Fang, Quantized anomalous Hall effect in magnetic topological insulators, *Science* **329**, 61 (2010).
 18. Y. Deng, Y. Yu, M. Z. Shi, J. Wang, X. H. Chen, and Y. Zhang, Magnetic-field-induced quantized anomalous Hall effect in intrinsic magnetic topological insulator MnBi_2Te_4 , arXiv:1904.11468

19. C. Liu, Y. Wang, H. Li, Y. Wu, Y. Li, J. Li, K. He, Y. Xu, J. Zhang, and Y. Wang, Quantum phase transition from axion insulator to Chern insulator in MnBi_2Te_4 , arXiv:1905.00715.
20. W. Luo and X. L. Qi, Massive Dirac surface states in topological insulator/magnetic insulator heterostructures, *Phys. Rev. B* **87**, 085431 (2013).
21. S. V. Eremeev, V. N. Men'shov, V. V. Tugushev, P. M. Echenique, and E. V. Chulkov, Magnetic proximity effect at the three-dimensional topological insulator/magnetic insulator interface, *Phys. Rev. B* **88**, 144430 (2013).
22. V. N. Men'shov, I. A. Shvets, and E. V. Chulkov, Interface effects on the magnetic-proximity-induced quantized Hall response in heterostructures based on three-dimensional topological insulators, *Phys. Rev. B* **99**, 115301 (2019).
23. C. X. Liu, X. L. Qi, X. Dai, Z. Fang, and S. C. Zhang, Quantum anomalous Hall effect in $\text{Hg}_{1-y}\text{Mn}_y\text{Te}$ quantum wells, *Phys. Rev. Lett.* **101**, 146802 (2008).
24. C. Z. Chang, J. Zhang, X. Feng, J. Shen, Z. Zhang, M. Guo, K. Li, Y. Ou, P. Wei, L. L. Wang *et al.* Experimental observation of the quantum anomalous Hall effect in a magnetic topological insulator, *Science* **340**, 167 (2013).

25. J. G. Checkelsky, R. Yoshimi, A. Tsukazaki, K. S. Takahashi, Y. Kozuka, J. Falson, M. Kawasaki, and Y. Tokura, Trajectory of the anomalous Hall effect towards the quantized state in a ferromagnetic topological insulator, *Nat. Phys.* **10**, 731 (2014).
26. C. Z. Chang, W. Zhao, D. Y. Kim, H. Zhang, B. A. Assaf, D. Heiman, S. C. Zhang, C. Liu, M. H. W. Chan, and J. S. Moodera, High-precision realization of robust quantum anomalous Hall state in a hard ferromagnetic topological insulator, *Nat. Mater.* **14**, 473 (2015).
27. S. Grauer, S. Schreyeck, M. Winnerlein, K. Brunner, C. Gould, and L. W. Molenkamp, Coincidence of superparamagnetism and perfect quantization in the quantum anomalous Hall state, *Phys. Rev. B* **92**, 201304(R) (2015).
28. A. J. Bestwick, E. J. Fox, X. Kou, L. Pan, K. L. Wang, and D. Goldhaber-Gordon, Precise quantization of the anomalous Hall effect near zero magnetic-field, *Phys. Rev. Lett.* **114**, 187201 (2015).
29. R. Watanabe, R. Yoshimi, M. Kawamura, M. Mogi, A. Tsukazaki, X. Z. Yu, K. Nakajima, K. S. Takahashi, M. Kawasaki, and Y. Tokura, Quantum anomalous Hall effect driven by magnetic proximity coupling in all-telluride based heterostructure, *Appl. Phys. Lett.* **115**, 102403 (2019).

30. X. Feng, Y. Feng, J. Wang, Y. Ou, Z. Hao, C. Liu, Z. Zhang, L. Zhang, C. Lin, J. Liao *et al.*, Thickness dependence of the quantum anomalous Hall effect in magnetic topological insulator films, *Adv. Mater.* **28**, 6386 (2016).
31. M. Salehi, H. Shapourian, I. T. Rosen, M. G. Han, J. Moon *et al.*, Quantum-Hall to insulator transition in ultra-low-carrier-density topological insulator films and a hidden phase of the zeroth Landau level, *Adv. Mater.* **31**, 1901091 (2019).
32. Y. S. Kim, M. Brahlek, N. Bansal, E. Edrey, G. A. Kapilevich, K. Iida, M. Tanimura, Y. Horibe, S. W. Cheong, and S. Oh, Thickness-dependent bulk properties and weak antilocalization effect in topological insulator Bi_2Se_3 , *Phys. Rev. B* **84**, 073109 (2011).
33. A. A. Taskin, S. Sasaki, K. Segawa, and Y. Ando, Manifestation of topological protection in transport properties of epitaxial Bi_2Se_3 thin films, *Phys. Rev. Lett.* **109**, 066803 (2012).
34. G. Landolt, S. Schreyeck, S. V. Eremeev, B. Slomski, S. Muff, J. Osterwalder, E. V. Chulkov, C. Gould, G. Karczewski, K. Brunner *et al.*, Spin texture of Bi_2Se_3 thin films in the quantum tunneling limit, *Phys. Rev. Lett.* **112**, 057601 (2014).

35. H. Zhang, C. X. Liu, X. L. Qi, X. Dai, Z. Fang, and S. C. Zhang, Topological insulators in Bi_2Se_3 , Bi_2Te_3 and Sb_2Te_3 with a single Dirac cone on the surface, *Nat. Phys.* **5**, 438 (2009).
36. Y. L. Chen, J. H. Chu, J. G. Analytis, Z. K. Liu, K. Igarashi, H. H. Kuo, X. L. Qi, S. K. Mo, R. G. Moore, D. H. Lu *et al.*, Massive Dirac fermion on the surface of a magnetically doped topological insulator, *Science* **329**, 659 (2010).
37. L. A. Wray, S. Y. Xu, Y. Xia, D. Hsieh, A. V. Fedorov, et al., A topological insulator surface under strong Coulomb, magnetic and disorder perturbations, *Nat. Phys.* **7**, 32 (2011).
38. M. R. Scholz, J. Sánchez-Barriga, D. Marchenko, A. Varykhalov, A. Volykhov et al., Tolerance of Topological Surface States towards Magnetic Moments: Fe on Bi_2Se_3 , *Phys. Rev. Lett.* **108**, 256810 (2012).
39. J. Honolka, A. A. Khajetoorians, V. Sessi, T. O. Wehling, S. Stepanow et al., In-Plane Magnetic Anisotropy of Fe Atoms on $\text{Bi}_2\text{Se}_3(111)$, *Phys. Rev. Lett.* **108**, 256811 (2012).

40. X. F. Kou, W. J. Jiang, M. R. Lang, F. X. Xiu, L. He, Y. Wang, Y. Wang, X. X. Yu, A. V. Fedorov, P. Zhang, and K. L. Wang, Magnetically doped semiconducting topological insulators, *J. Appl. Phys.* **112**, 063912 (2012).
41. M. Brahlek, N. Koirala, M. Salehi, N. Bansal, and S. Oh, Emergence of decoupled surface transport channels in bulk insulating Bi_2Se_3 thin films, *Phys. Rev. Lett.* **113**, 026801 (2014).
42. Y. Y. Li, G. Wang, X. G. Zhu, M. H. Liu, C. Ye, X. Chen, Y. Y. Wang, K. He, L. L. Wang, X. C. Ma *et al.*, Intrinsic topological insulator Bi_2Te_3 thin films on Si and their thickness limit, *Adv. Mater.* **22**, 4002 (2010).
43. See Supplementary Materials for additional information on experimental methods, characterization of electronic band structure by ARPES, detailed data of electric transport measurements, calculated band structure, and structural characterization.
44. Y. Satake, J. Shiogai, D. Takane, K. Yamada, K. Fujiwara, S. Souma, T. Sato, T. Takahashi, and A. Tsukazaki, Fermi-level tuning of the Dirac surface state in $(\text{Bi}_{1-x}\text{Sb}_x)_2\text{Se}_3$ thin films, *J. Phys.: Condens. Matter* **30**, 085501 (2018).

- 45. Y. Satake, J. Shiogai, K. Fujiwara, and A. Tsukazaki, Effect of the depletion region in topological insulator heterostructures for ambipolar field-effect transistors, *Phys. Rev. B* **98**, 125415 (2018).
- 46. J. M. Zhang, W. Zhu, Y. Zhang, D. Xiao, and Y. Yao. Tailoring Magnetic Doping in the Topological Insulator Bi_2Se_3 , *Phys. Rev. Lett.* **109**, 266405 (2012).
- 47. M. G. Vergniory, M. M. Otrokov, D. Thonig, M. Hoffmann, I. V. Maznichenko, et al., Exchange interaction and its tuning in magnetic binary chalcogenides, *Phys. Rev. B* **89**, 165202 (2014).
- 48. P. A. Lee and T. V. Ramakrishnan. Disordered electronic systems, *Rev. Mod. Phys.* **57**, 287 (1985).
- 49. E. Abrahams, S. V. Kravchenko, and M. P. Sarachik, Metallic behavior and related phenomena in two dimensions, *Rev. Mod. Phys.* **73**, 251 (2001).
- 50. J. Liao, Y. Ou, X. Feng, S. Yang, C. Lin, W. Yang, K. Wu, K. He, X. Ma, Q. K. Xue, and Y. Li, Observation of Anderson localization in ultrathin films of three-dimensional topological insulators, *Phys Rev. Lett.* **114**, 216601 (2015).

51. C. X. Liu, H. J. Zhang, B. Yan, X. L. Qi, T. Frauenheim, X. Dai, Z. Fang, and S. C. Zhang, Oscillatory crossover from two-dimensional to three-dimensional topological insulators, *Phys. Rev. B* **81**, 041307(R) (2010).
52. K. Kobayashi, Y. Yoshimura, K. I. Imura, and T. Ohtsuki, Dimensional crossover of transport characteristics in topological insulator nanofilms, *Phys. Rev. B* **92**, 235407 (2015).
53. M. Liu, J. Zhang, C. Z. Chang, Z. Zhang, X. Feng, *et al.*, Crossover between Weak Antilocalization and Weak Localization in a Magnetically Doped Topological Insulator, *Phys. Rev. Lett.* **108**, 036805 (2012).
54. K. Nomura and N. Nagaosa, Surface-quantized anomalous Hall current and the magnetoelectric effect in magnetically disordered topological insulators, *Phys. Rev. Lett.* **106**, 166802 (2011).
55. M. Mogi, R. Yoshimi, A. Tsukazaki, K. Yasuda, Y. Kozuka, K. S. Takahashi, M. Kawasaki, and Y. Tokura, Magnetic modulation doping in topological insulators toward higher-temperature quantum anomalous Hall effect, *Appl. Phys. Lett.* **107**, 182401 (2015).
56. S. Grauer, K. M. Fijalkowski, S. Schreyeck, M. Winnerlein, K. Brunner, R.

- Thomale, C. Gould, and L. W. Molenkamp, Scaling of the quantum anomalous Hall effect as an indicator of axion electrodynamics, *Phys. Rev. Lett.* **118**, 246801 (2017).
57. J. G. Analytis, R. D. McDonald, S. C. Riggs, J. H. Chu, G. S. Boebinger, and I. R. Fisher, Two-dimensional surface state in the quantum limit of a topological insulator, *Nat. Phys.* **6**, 960 (2010).
58. Y. S. Fu, T. Hanaguri, K. Igarashi, M. Kawamura, M. S. Bahramy, and T. Sasagawa, Observation of Zeeman effect in topological surface state with distinct material dependence, *Nat. Commun.* **7**, 10829 (2016).
59. J. G. Rousset, J. Papierska, W. Pacuski, A. Golnik, M. Nawrocki, W. Stefanowicz, S. Stefanowicz, M. Sawicki, R. Jakieła, T. Dietl *et al.*, Relation between exciton splittings, magnetic circular dichroism, and magnetization in wurtzite $\text{Ga}_{1-x}\text{Fe}_x\text{N}$, *Phys. Rev. B* **88**, 115208 (2013).

Figure legends

FIG. 1 Schematic and calculated electronic band structure. (a-c) Evolution of surface spin subband structure in paramagnetic Fe-doped $(\text{Bi,Sb})_2\text{Se}_3$ thin films upon thickness reduction and external magnetic field application. (a) Surface states of spin-up (magenta) and spin-down (cyan) subbands with gap Δ_{hy} driven by inter-surface hybridization, leading to 2D insulator phase. (b) Under an external perpendicular magnetic field, the spin subband degeneracy is lifted by the Zeeman effect, producing band crossing when the Zeeman energy Δ_{Zeeman} exceeds Δ_{hy} . (c) At crossings of spin up (magenta) and spin down (cyan) bands, a gap is generated by the spin-orbit interaction, leaving a one-dimensional chiral edge channel in the bulk bandgap (red solid line). (d-f) Calculated band structure of three-dimensional topological insulator thin films. The band structure is calculated using the 3D-TI slab for cases in which (d) Δ_{hy} is larger than Δ_{Zeeman} , (e) Δ_{hy} is comparable to Δ_{Zeeman} , and (f) Δ_{Zeeman} is larger than Δ_{hy} . (g) ARPES intensity of the 30-nm-thick $\text{Fe}_{0.05}(\text{Bi}_{0.34}\text{Sb}_{0.66})_{1.95}\text{Se}_3$ /3-nm-thick Bi_2Se_3 film around the $\overline{\Gamma}$ point measured at $T = 40$ K. SS and VB respectively represent surface state and bulk valence band. E_F is indicated by a white dashed line. (h) Longitudinal resistance R_{xx} of $\text{Fe}_{0.05}(\text{Bi}_{0.34}\text{Sb}_{0.66})_{1.95}\text{Se}_3/\text{Bi}_2\text{Se}_3$ at $B = 0$ as a function of the magnetic layer thickness d and temperature T . Colour bar scale is in the units of h/e^2 . (i) Magnetoresistance of

$\text{Fe}_{0.05}(\text{Bi}_{0.34}\text{Sb}_{0.66})_{1.95}\text{Se}_3/\text{Bi}_2\text{Se}_3$ at 2 K as a function of d and B . Colour scale bar corresponds to +20 (blue) to −100 (red) %.

FIG. 2 Hall resistance of Fe-doped and non-magnetic heterostructures against Sb composition y at 9 T and 2 K. Hall resistances R_{yx} of 14-nm-thick $\text{Fe}_x(\text{Bi}_{1-y}\text{Sb}_y)_{2-x}\text{Se}_3/3$ -nm-thick Bi_2Se_3 (red circles) dominated by the anomalous component and of 14–20-nm-thick non-magnetic $(\text{Bi}_{1-y}\text{Sb}_y)_2\text{Se}_3/3$ -nm-thick Bi_2Se_3 films (black squares) are shown against Sb content y . CNP denotes the charge neutral point of non-magnetic samples. The inset shows the Hall effect measurement for $\text{Fe}_x(\text{Bi}_{0.33}\text{Sb}_{0.67})_{2-x}\text{Se}_3/3$ -nm-thick Bi_2Se_3 films for Fe content $x = 0$ (solid black line), 0.04 (orange), and 0.05 (red).

FIG. 3 Magnetic-field-induced insulator-metal transition and quantum anomalous Hall effect. (a) Longitudinal sheet resistance $R_{xx}(T)$ of 14-nm-thick $\text{Fe}_{0.05}(\text{Bi}_{0.33}\text{Sb}_{0.67})_{1.95}\text{Se}_3/\text{Bi}_2\text{Se}_3$ heterostructure (inset) in various magnetic fields B . (b) Hall and sheet resistances, $R_{yx}(B)$ (solid red line) and $R_{xx}(B)$ (solid black line), measured for a FET device (shown in the inset) at $V_G = -60$ V and $T = 1.6$ K. The R_{yx} data below 1 T were not obtained owing to the large value of R_{xx} .

FIG. 4 Magnetic-field-induced insulator-QAH phase transition. (a,b) Temperature dependences of the longitudinal and Hall conductivities (σ_{xx} and σ_{xy}) at $V_G = -60$ V for various magnetic fields B . (c) Renormalization group flow in the $[\sigma_{xx}(T), \sigma_{xy}(T)]$ plane in various B from 3 to 15 T. Each curve is extracted from data in (a) and (b) employing the same colour code. Empty and filled circles respectively present data obtained at $T = 15$ and 1.6 K. The $[\sigma_{xx}, \sigma_{xy}]$ flow extracted from the data as a function of the magnetic field at $T = 1.6$ K is also shown (solid black line).

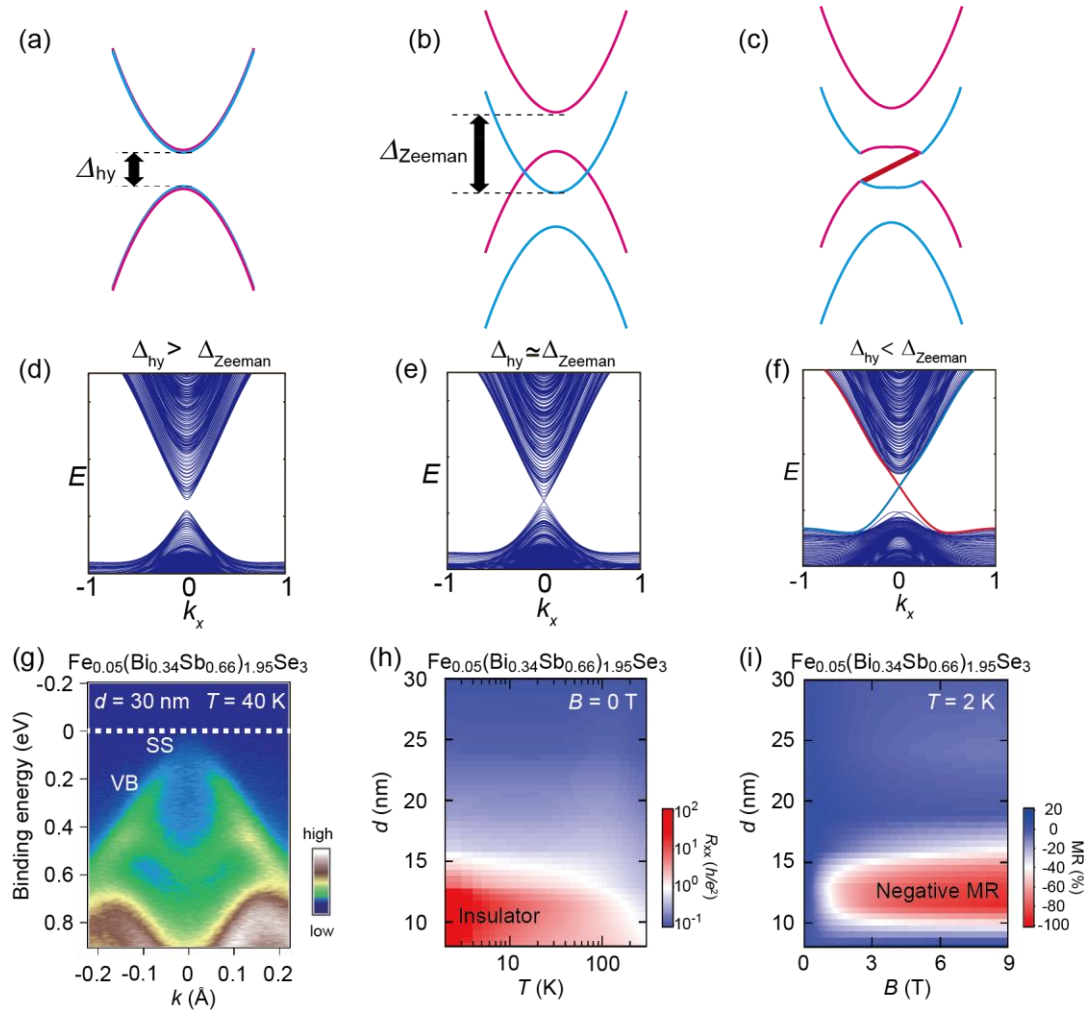


Figure 1 Y. Satake *et al.*

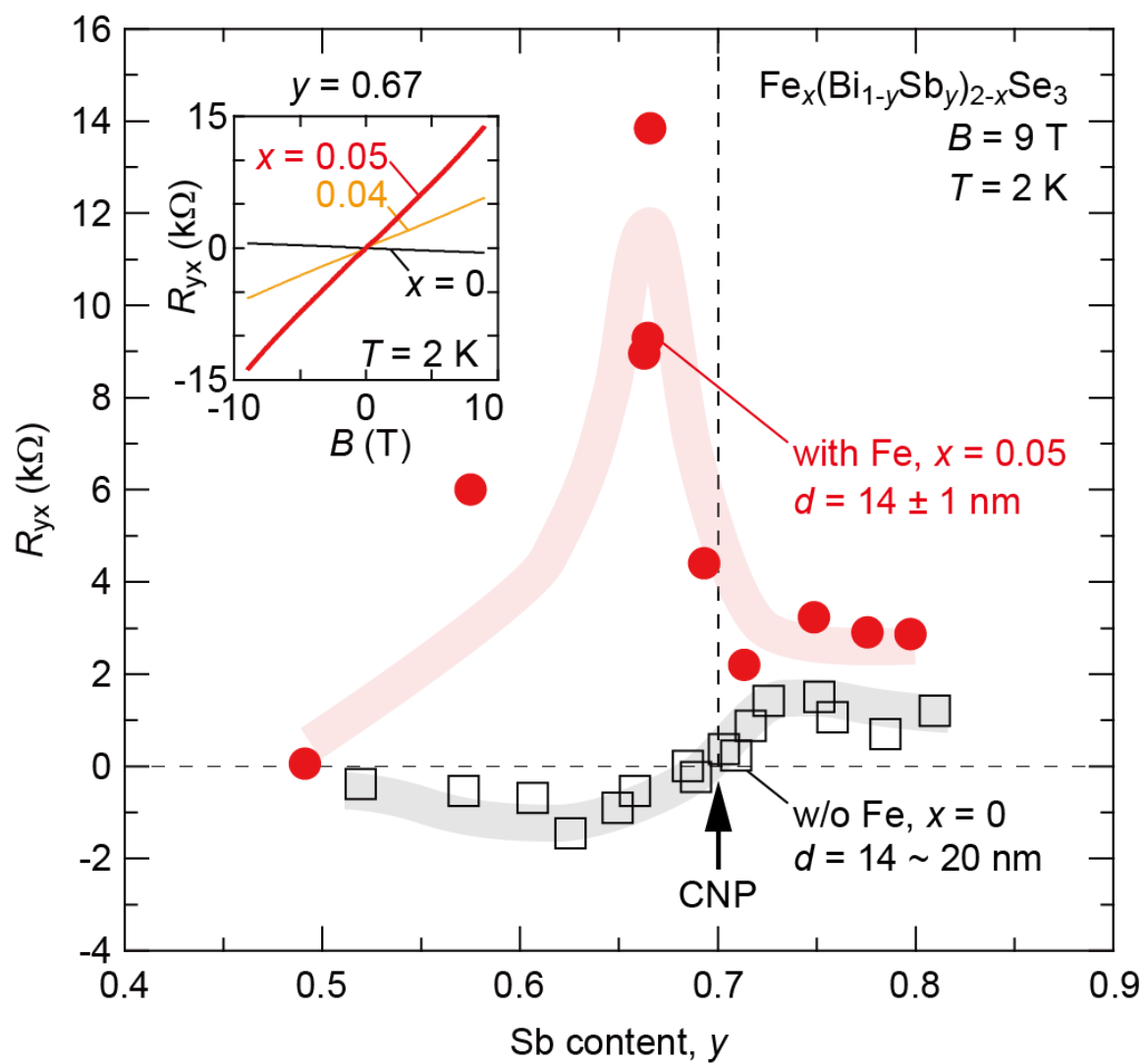


Figure 2 Y. Satake *et al.*

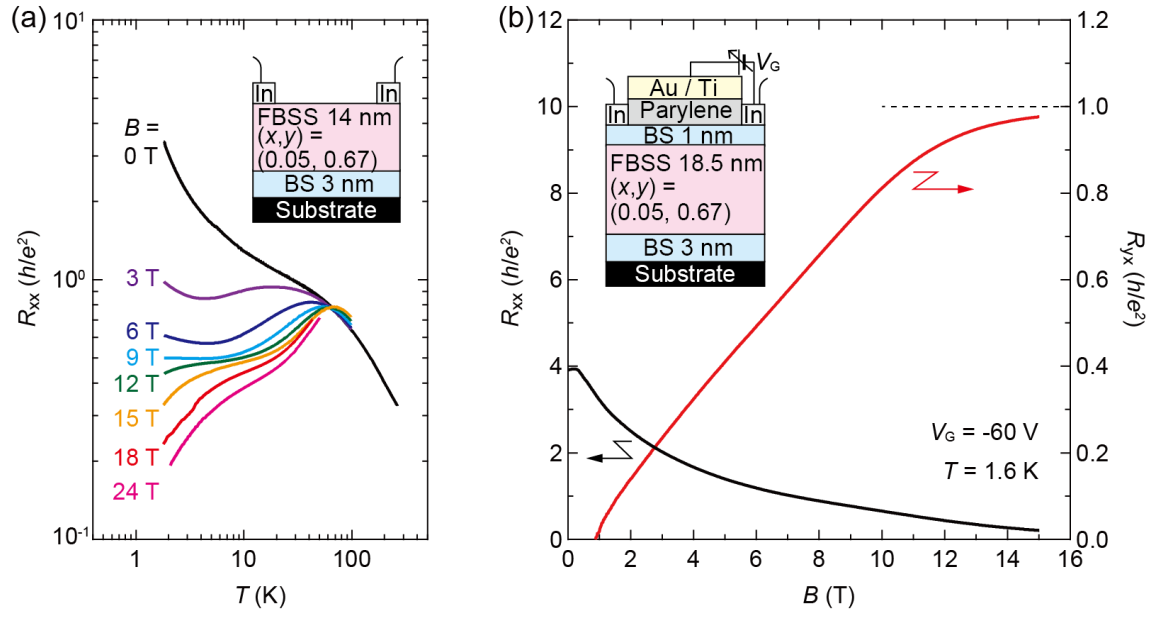


Figure 3 Y. Satake *et al.*

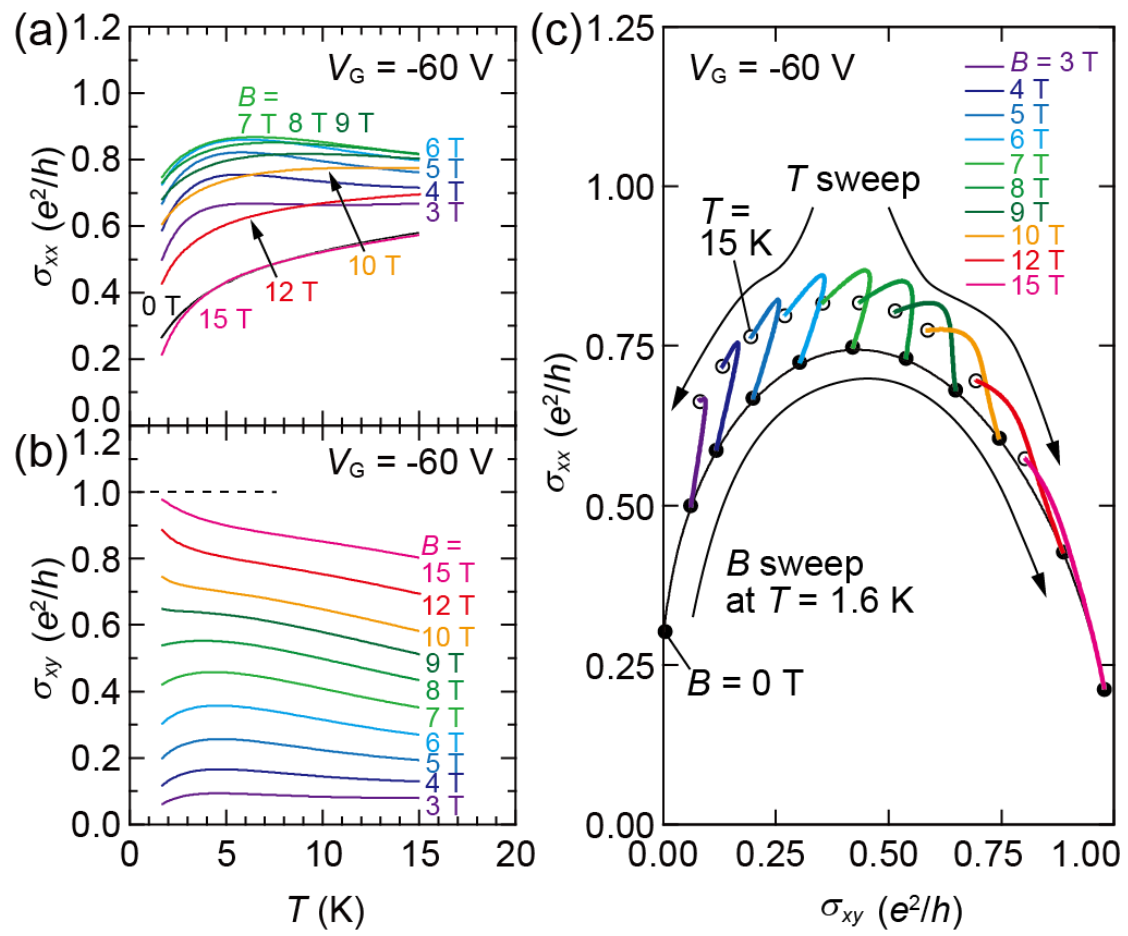


Figure 4 Y. Satake *et al.*

Supplementary Materials for
Magnetic-field-induced topological phase transition in Fe-doped
(Bi,Sb)₂Se₃ heterostructures

Y. Satake^{1,2}, J. Shiogai^{1*}, G. P. Mazur², S. Kimura¹, S. Awaji¹, K. Fujiwara¹,
T. Nojima¹, K. Nomura^{1,3}, S. Souma^{3,4}, T. Sato^{3,4,5}, T. Dietl^{2,4} and A. Tsukazaki^{1,3}

¹*Institute for Materials Research, Tohoku University, Sendai 980-8577, Japan*

²*International Research Centre MagTop, Institute of Physics, Polish Academy of
Sciences, Aleja Lotnikow 32/46, PL-02668 Warsaw, Poland*

³*Center for Spintronics Research Network (CSRN), Tohoku University, Sendai 980-8577,
Japan*

⁴*WPI-Advanced Institute for Materials Research, Tohoku University, Sendai 980-8577,
Japan*

⁵*Department of Physics, Tohoku University, Sendai 980-8578, Japan*

*Author to whom correspondence should be addressed.

Electronic mail: junichi.shiogai@imr.tohoku.ac.jp

Contents

1. Experimental details.
2. Hall resistance of $\text{Fe}_x(\text{Bi}_{0.33}\text{Sb}_{0.67})_{2-x}\text{Se}_3/\text{Bi}_2\text{Se}_3$ bilayers with various Fe contents x .
3. Electronic band structure of $\text{Fe}_{0.05}(\text{Bi}_{0.34}\text{Sb}_{0.66})_{1.95}\text{Se}_3$ from ARPES.
4. Temperature and magnetic-field dependence of transport properties for various $\text{Fe}_{0.05}(\text{Bi}_{0.34}\text{Sb}_{0.66})_{1.95}\text{Se}_3$ layer thicknesses.
5. Hybridization effects in non-magnetic and magnetic topological heterostructures
6. Magneto-transport properties in perpendicular and in-plane magnetic fields.
7. $R_{xx}(B)$ and $R_{yx}(B)$ measured for the FET device for various gate voltages V_G .
8. $R_{xx}(T)$ and $R_{yx}(T)$ measured for the FET device under various magnetic fields.
9. Estimation of energies accounting for band crossing in Fe-doped $(\text{Bi,Sb})_2\text{Se}_3/\text{Bi}_2\text{Se}_3$ bilayer.
10. Gate voltage dependence of $R_{xx}(B)$ and $R_{yx}(B)$ in a field-effect transistor (FET) based on the trilayer structure.
11. Structural analysis.

1. Experimental details

1-1. Thin-film growth

Heterostructures consisting of $\text{Fe}_x(\text{Bi}_{1-y}\text{Sb}_y)_{2-x}\text{Se}_3$ layers with various thicknesses d deposited onto 3-nm-thick Bi_2Se_3 buffer layer and trilayer structures consisting of 1-nm-thick Bi_2Se_3 /18.5-nm-thick $\text{Fe}_x(\text{Bi}_{1-y}\text{Sb}_y)_{2-x}\text{Se}_3$ /3-nm-thick Bi_2Se_3 were synthesized using molecular-beam epitaxy (MBE) on semi-insulating InP(111) substrates at 250°C. The flux of each element is characterized by the beam equivalent pressure. During the growth, Bi and Se fluxes were fixed at 3.5×10^{-6} Pa and 1.7×10^{-4} Pa, respectively, whereas Fe and Sb fluxes were varied depending on the desired contents. The Sb composition is calibrated using electron energy dispersive x-ray spectroscopy (EDX) and Rutherford back scattering (RBS) [1]. The Fe composition is estimated using the flux ratio. We regard the most favorable site of Fe as cation substitution [2,3]. Film thicknesses were ascertained from the Laue thickness fringes in x-ray diffraction patterns.

1-2. ARPES measurements

The films were transferred from the MBE chamber to the ARPES apparatus immediately after their growth. To transfer samples without breaking ultrahigh vacuum, we use a portable chamber that maintains ultrahigh vacuum. The base pressure of the portable chamber was kept below 7×10^{-7} Pa. Measurements were taken at Tohoku University with a MBS A1 electron analyzer using a high-flux He discharge lamp and a toroidal grating monochromator. The He I α ($h\nu = 21.218$ eV) line was used to excite photoelectrons.

1-3. FET device fabrication

The sample was patterned into Hall-bar geometry using standard photolithography and wet chemical etching. After etching, gate dielectric of 180-nm-thick parylene was deposited at room temperature, followed by the deposition of Au (100 nm)/Ti (10 nm) as a gate electrode. The channel width and center-to-center separation between longitudinal voltage probes were both approximately 100 μm . We adopted 1-nm-thick Bi_2Se_3 /18.5-nm-thick $\text{Fe}_x(\text{Bi}_{1-y}\text{Sb}_y)_{2-x}\text{Se}_3$ /3-nm-thick Bi_2Se_3 trilayer structure as a channel of the FET device. We expect that the top undoped Bi_2Se_3 capping layer suppresses disorder on the top of Dirac surface states possibly induced by Fe doping. Furthermore, the nearly symmetric structure consisting of 1-nm-thick Bi_2Se_3 /18.5-nm-thick $\text{Fe}_x(\text{Bi}_{1-y}\text{Sb}_y)_{2-x}\text{Se}_3$ /3-nm-thick Bi_2Se_3 trilayer cancels the energy differences of the Dirac points formed on the top and bottom surface states and depletes bulk carriers. Under the assumption that the number of hole carriers in 14-nm-thick $\text{Fe}_{0.05}(\text{Bi}_{0.33}\text{Sb}_{0.67})_{1.95}\text{Se}_3$ is almost equal to that of the electrons in 3-nm-thick Bi_2Se_3 bilayer, we increased the thickness of $\text{Fe}_{0.05}(\text{Bi}_{0.33}\text{Sb}_{0.67})_{1.95}\text{Se}_3$ to 18.5 nm to compensate for the effect of excessive electrons brought by deposition of the top 1-nm-thick Bi_2Se_3 .

1-4. Transport measurements

For electrical transport measurements, samples were examined using a Physical Property Measurement System (Quantum Design), a ^4He variable temperature insert equipped with a 15-Tesla superconducting magnet (Oxford Instruments plc.), or a 25 T Cryogen-free Superconducting Magnet (CSM) installed at High Field Laboratory for Superconducting Materials of Institute for Materials Research (IMR), Tohoku

University, Japan [4]. The longitudinal sheet resistance and Hall resistance were measured using standard lock-in technique with a typical excitation current of 10 nA and a repetition rate of 13 Hz. Electrical contacts were made using an indium solder. To exclude geometric effects, the measured data were symmetrized for R_{xx} and anti-symmetrized for R_{yx} against B .

2. Hall resistance of $\text{Fe}_x(\text{Bi}_{0.33}\text{Sb}_{0.67})_{2-x}\text{Se}_3/\text{Bi}_2\text{Se}_3$ bilayers with various Fe content x .

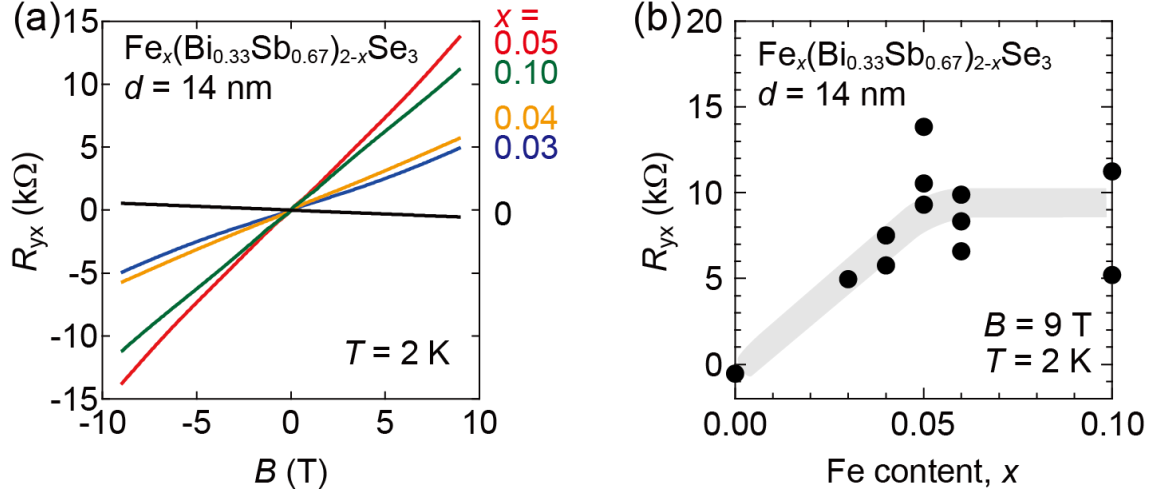


FIG. S1. Hall resistance of $\text{Fe}_x(\text{Bi}_{0.33}\text{Sb}_{0.67})_{2-x}\text{Se}_3/\text{Bi}_2\text{Se}_3$ bilayers with various Fe contents x and magnetic layer thickness $d = 14$ nm. (a) Hall resistance R_{yx} as a function of the magnetic field B at 2 K of $\text{Fe}_x(\text{Bi}_{0.33}\text{Sb}_{0.67})_{2-x}\text{Se}_3/\text{Bi}_2\text{Se}_3$ bilayers with $x = 0$ (black), 0.03 (blue), 0.04 (yellow), 0.05 (red), and 0.10 (green). (b) R_{yx} at 2 K and 9 T for $\text{Fe}_x(\text{Bi}_{0.33}\text{Sb}_{0.67})_{2-x}\text{Se}_3/\text{Bi}_2\text{Se}_3$ bilayers as a function of Fe content x .

Figure S1(a) presents results of Hall effect measurements at $T = 2$ K for $\text{Fe}_x(\text{Bi}_{0.33}\text{Sb}_{0.67})_{2-x}\text{Se}_3/\text{Bi}_2\text{Se}_3$ bilayers with $x = 0, 0.03, 0.04, 0.05$, and 0.10 and magnetic layer thickness of $d = 14$ nm. The Bi_2Se_3 buffer layer thickness is 3 nm for all studied samples. The top layer thickness of $d = 14$ nm is chosen to maximize R_{yx} for $\text{Fe}_x(\text{Bi}_{0.33}\text{Sb}_{0.67})_{2-x}\text{Se}_3$ with $x = 0.05$. Large positive slopes of $R_{yx}(B)$ are observed in Fe-doped samples, which constitute evidence that a large anomalous Hall term is generated by Fe doping. Figure S1(b) displays R_{yx} at $T = 2$ K and in $B = 9$ T as a function of Fe content x . With increasing Fe content, R_{yx} in $B = 9$ T tends to increase

linearly up to $x = 0.05$ and to saturate for larger x . This saturation suggests the solubility limit of Fe.

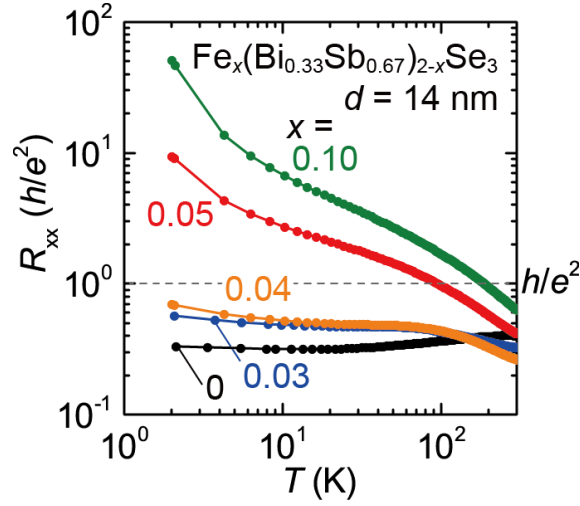


Figure S2 | Temperature dependence of the sheet resistance in $\text{Fe}_x(\text{Bi}_{0.33}\text{Sb}_{0.67})_{2-x}\text{Se}_3/\text{Bi}_2\text{Se}_3$ bilayer for various Fe content x .

Figure S2 shows corresponding temperature dependence of the sheet resistance $R_{xx}(T)$. With increasing Fe concentration, the metallic behavior for $x = 0$ turns into an insulating behavior in $x > 0.05$. Therefore, for 14-nm-thick $\text{Fe}_x(\text{Bi}_{0.33}\text{Sb}_{0.67})_{2-x}\text{Se}_3/3\text{-nm Bi}_2\text{Se}_3$ bilayer structure, the critical Fe concentration causing the Anderson insulator seems to be $x = 0.05$.

3. Electronic band structure of $\text{Fe}_{0.05}(\text{Bi}_{0.34}\text{Sb}_{0.66})_{1.95}\text{Se}_3$ from ARPES.

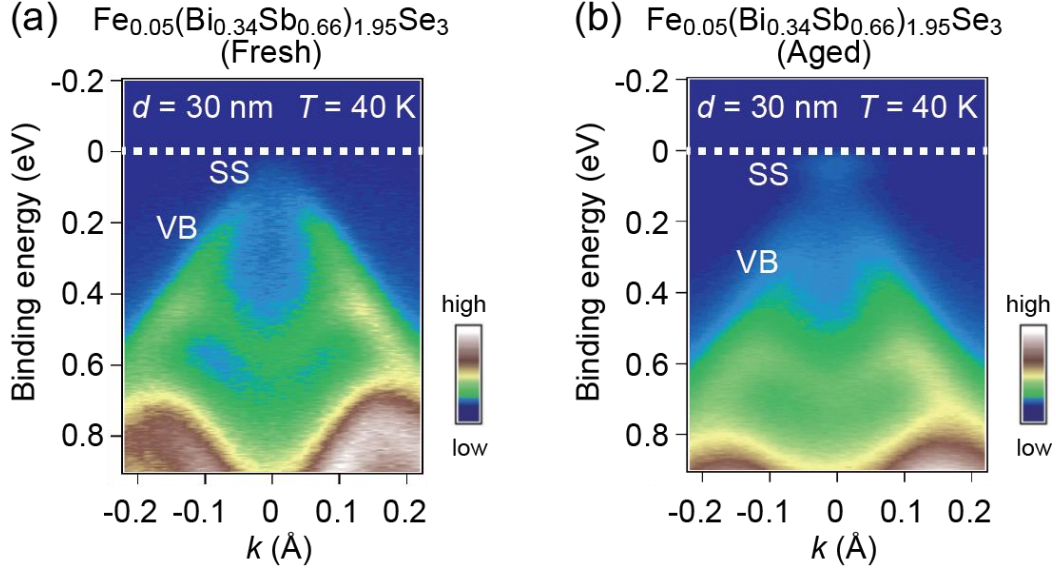


FIG. S3. Band structure of $\text{Fe}_{0.05}(\text{Bi}_{0.34}\text{Sb}_{0.66})_{1.95}\text{Se}_3$ from ARPES measurements. (a,b) ARPES results for the 30-nm-thick $\text{Fe}_{0.05}(\text{Bi}_{0.34}\text{Sb}_{0.66})_{1.95}\text{Se}_3$ layer on top of the Bi_2Se_3 buffer layer around the $\bar{\Gamma}$ point (a) before and (b) after surface aging. SS and VB respectively represent surface and bulk valence bands.

Figure S3(a) (corresponding to Fig. 1(g) in the main text) shows the electronic band structure along the $\bar{\Gamma} - \bar{K}$ cut of a $\text{Fe}_{0.05}(\text{Bi}_{0.34}\text{Sb}_{0.66})_{1.95}\text{Se}_3/\text{Bi}_2\text{Se}_3$ bilayer with magnetic layer thickness of $d = 30$ nm. The Fermi level is located slightly above the valence band. To study the surface band further, we have used the surface aging technique that increases band bending and shifts the Fermi level up, as shown in Fig. S3(b). In this manner, we visualize the linear dispersion and the Dirac point in the surface band. No gap at the Dirac point is detectable at this energy resolution, top layer thickness, and Fe concentration. In addition, compared to the data for a $(\text{Bi,Sb})_2\text{Se}_3$ film

[1], no discernible differences are detectable in the band structure and surface dispersion.

4. Temperature and magnetic-field dependence of transport properties for various $\text{Fe}_{0.05}(\text{Bi}_{0.34}\text{Sb}_{0.66})_{1.95}\text{Se}_3$ layer thicknesses.

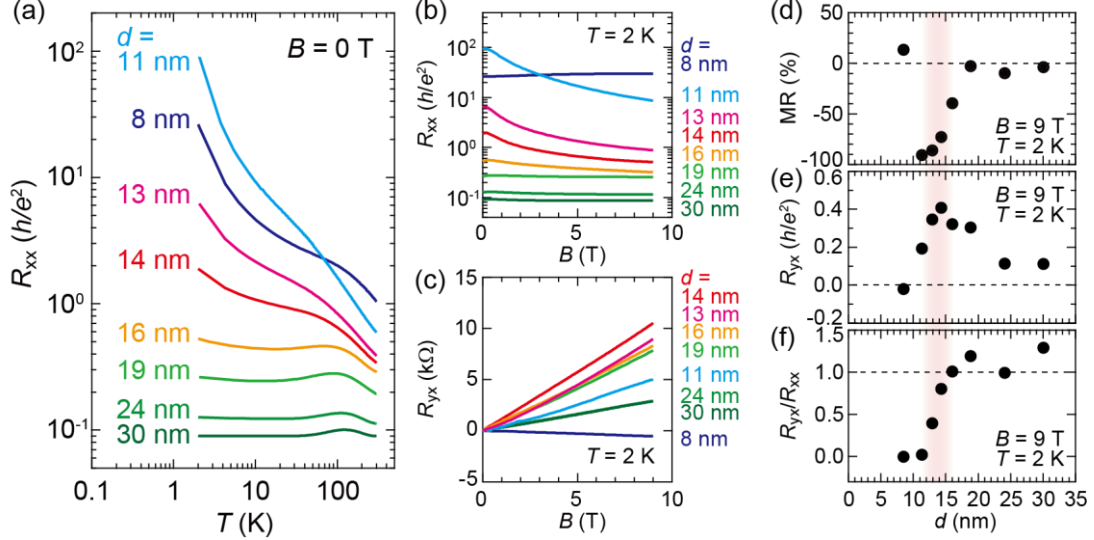


FIG. S4. Temperature and magnetic-field dependence of transport properties for $\text{Fe}_{0.05}(\text{Bi}_{0.34}\text{Sb}_{0.66})_{1.95}\text{Se}_3/\text{Bi}_2\text{Se}_3$ bilayers with various magnetic layer thickness d . (a) $R_{xx}(T)$ measured in $B = 0$, and (b) $R_{xx}(B)$ and (c) $R_{yx}(B)$ measured at $T = 2$ K for various magnetic layer thicknesses d of 8 nm (blue) to 30 nm (green). Thickness dependences of (d) magneto-resistance ratio [defined as $\text{MR} = R_{xx}(B)/R_{xx}(0) - 1$], (e) R_{yx} and (f) the Hall angle R_{yx}/R_{xx} in $B = 9$ T and at $T = 2$ K.

Figure S4(a) shows the raw dataset of $R_{xx}(T)$, as presented in Fig. 1(h) in the main text for $\text{Fe}_{0.05}(\text{Bi}_{0.34}\text{Sb}_{0.66})_{1.95}\text{Se}_3/\text{Bi}_2\text{Se}_3$ bilayers in $B = 0$ T with the magnetic layer thickness d varying from 8 nm (solid blue line) to 30 nm (solid green line). A metal-to-insulator transition occurs with decreasing d . Figures S4(b) and S4(c) present raw datasets $R_{xx}(B)$ and $R_{yx}(B)$ taken at 2 K, presented in Fig. 1(i) in the main text, for $\text{Fe}_{0.05}(\text{Bi}_{0.34}\text{Sb}_{0.66})_{1.95}\text{Se}_3/\text{Bi}_2\text{Se}_3$ bilayers with the magnetic layer thicknesses of 8 nm to

30 nm. Magnetoresistance ratio MR, R_{yx} and the Hall angle R_{yx}/R_{xx} in $B = 9$ T are presented respectively in Figs. S4(d) – S4(f). Magnitudes of both negative MR and positive R_{yx} attain maximum values around $d = 14$ nm, as shown by the red shaded area. Note that a small positive MR and negative R_{yx} for $d = 8$ nm originates from a remanent bulk conduction in bottom n -type Bi_2Se_3 where bulk carriers are not fully depleted by top p -type $\text{Fe}_{0.05}(\text{Bi}_{0.34}\text{Sb}_{0.66})_{1.95}\text{Se}_3/\text{Bi}_2\text{Se}_3$ layer [5].

5. Hybridization effects in non-magnetic and magnetic topological heterostructures.

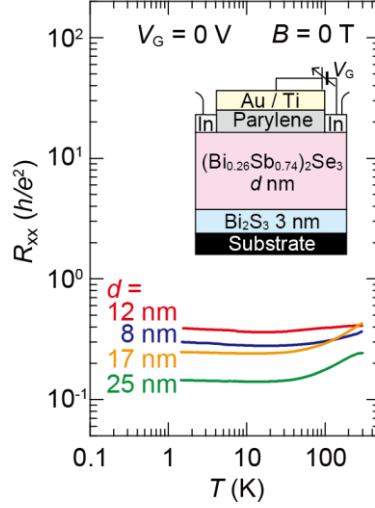


FIG. S5. Temperature dependence of sheet resistance $R_{xx}(T)$ of field-effect transistors based on $(\text{Bi}_{0.26}\text{Sb}_{0.74})_2\text{Se}_3/\text{Bi}_2\text{Se}_3$ bilayer. Sheet resistance $R_{xx}(T)$ in a zero magnetic field and gate voltage for field effect transistors consisting of a 3 nm thick Bi_2Se_3 buffer layer and non-magnetic $(\text{Bi}_{0.26}\text{Sb}_{0.74})_2\text{Se}_3$ layers with thicknesses $d = 8$ (blue), 12 (red), 17 (orange), and 25 nm (green) [5].

5-1. $(\text{Bi}_{0.26}\text{Sb}_{0.74})_2\text{Se}_3/\text{Bi}_2\text{Se}_3$ bilayers

Because of hybridization between top and bottom surfaces, a gap opens at the Dirac point in TI films of the thicknesses below a critical value [6-11]. Figure S5 presents $R_{xx}(T)$ in $B = 0$ and at $V_G = 0$ for field-effect transistors of $(\text{Bi}_{0.26}\text{Sb}_{0.74})_2\text{Se}_3/\text{Bi}_2\text{Se}_3$ bilayers with the non-magnetic $(\text{Bi}_{0.26}\text{Sb}_{0.74})_2\text{Se}_3$ layer thickness varying from 8 (blue) to 25 nm (green). Data are extracted from our earlier report [5].

All devices show metallic behavior indicating that hybridization effects are not appreciable down to the 8 nm thickness in non-Fe-doped heterostructures even if the Fermi level is close to the neutrality point.

5-2. Earlier studies of Bi₂Se₃, Bi₂Te₃, Sb₂Te₃, and (Bi,Sb)₂Te₃ films

The critical thicknesses found using angle-resolved photoemission spectroscopy are approximately five quintuple layers (QL) [6] (one QL corresponds to approximately 1 nm), 1 QL [7], and 4 QL [9], respectively, for Bi₂Se₃, Bi₂Te₃, and Sb₂Te₃. For a (Bi,Sb)₂Te₃ thin film, the critical thickness is apparently less than 5 QL, because no gap is formed at this thickness [12].

5-3. 3d transition metal-doped Bi₂Se₃ and (Bi,Sb)₂Te₃ films

Reportedly, the respective critical thicknesses of the Cu-doped Bi₂Se₃ and the Cr-doped (Bi,Sb)₂Te₃-based heterostructures are approximately 10 nm [13] and 13 nm [14]. These values are larger than the critical thicknesses of Bi₂Se₃ and (Bi,Sb)₂Te₃, respectively. The penetration depths of surface states ξ are related directly to surface hybridization according to $\xi = \hbar v_F / |M|$, where v_F is the Fermi velocity and $|M|$ is the charge excitation gap [15]. The ξ magnitude can increase by doping with light elements, which decreases the spin-orbit interaction and consequently reduces $|M|$ [16,17]. A larger value of the critical thickness might derive from reduction of the spin-orbit interaction by 3d transition metal doping. Therefore, it is plausible that the Fe-doped (Bi,Sb)₂Se₃ layer critical thickness is enhanced over the values reported for

non-magnetic TIs. We present information for the critical thicknesses of various compounds in Table S1.

Compounds	Critical thickness	Method	Reference
Bi_2Se_3	5 QL	Spectroscopy	ref. 6
Bi_2Te_3	1 QL	Spectroscopy	ref. 7
Sb_2Te_3	3 QL	Spectroscopy	ref. 9
$(\text{Bi,Sb})_2\text{Te}_3$	< 5 QL	Spectroscopy	ref. 12
Cu-doped Bi_2Se_3	> 10 QL	Transport	ref. 13
Cr-doped $(\text{Bi,Sb})_2\text{Te}_3$ based heterostructure	> 13 QL	Transport	ref. 14

Table S1. Collection of critical thicknesses at which top and bottom surface states hybridize for various compounds.

6. Magneto-transport properties in perpendicular and in-plane magnetic fields.

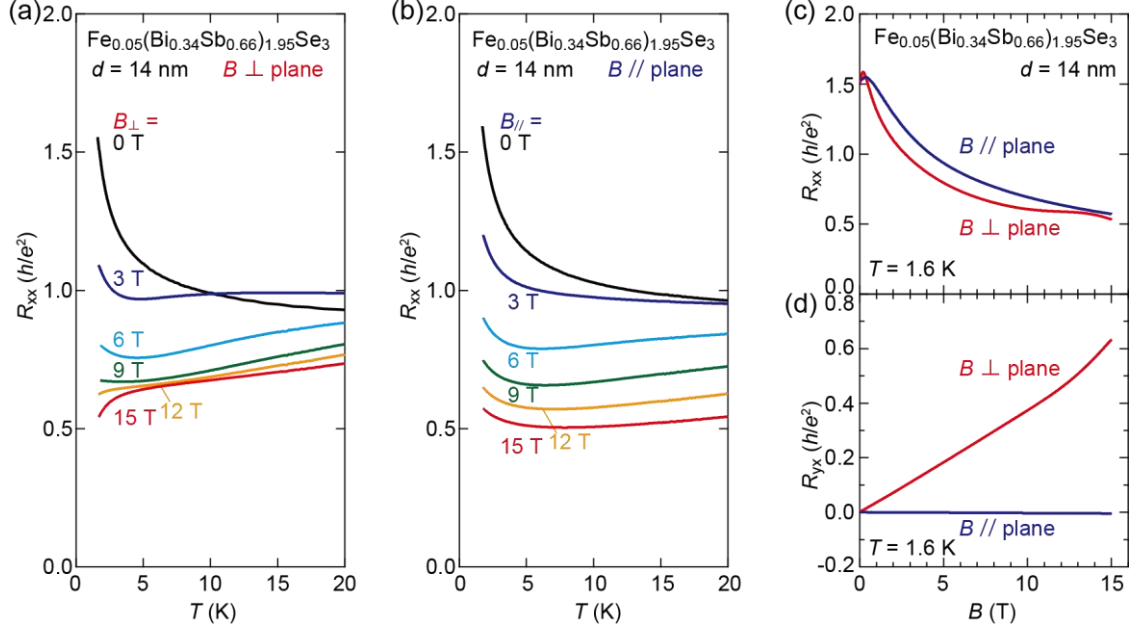


FIG. S6. Role of the magnetic field orientation. (a,b) $R_{xx}(T)$ dependencies for a $\text{Fe}_{0.05}(\text{Bi}_{0.34}\text{Sb}_{0.66})_{1.95}\text{Se}_3/\text{Bi}_2\text{Se}_3$ bilayer with the magnetic layer thickness $d = 14$ nm in various magnetic fields B . The magnetic field is applied (a) perpendicularly to the sample plane and (b) in-plane. (c,d) $R_{xx}(B)$ and $R_{yx}(B)$ dependencies in perpendicular (red curves) and in-plane (blue curves) magnetic fields at $T = 1.6$ K for the same sample.

To explore characteristic of the field-induced topological phase transitions further, we studied transport properties for two orientations of the magnetic field with respect to the film plane. Figure S6 shows $R_{xx}(T)$ in perpendicular (Fig. S6(a)) and in-plane (Fig. S6(b)) magnetic fields for a $\text{Fe}_{0.05}(\text{Bi}_{0.34}\text{Sb}_{0.66})_{1.95}\text{Se}_3/\text{Bi}_2\text{Se}_3$ bilayer with magnetic layer thickness $d = 14$ nm. A similar magnitude of negative magnetoresistance is observed for the two field directions in the high-temperature region, substantiating the role of the

magnetic field in reducing scattering by Fe spins. At low temperatures, however, the insulator-to-metal transition is observed only by application of an out-of-plane magnetic field, whereas the insulating behaviour [$dR_{xx}(T)/dT < 0$] remains under the in-plane magnetic field of 15 T. Therefore, metallization is observed only when the magnetic field is applied perpendicular to the film plane, which substantiates our claim that the quantum phase transition occurs from the 2D-insulator to the quantum anomalous Hall state.

7. $R_{xx}(B)$ and $R_{yx}(B)$ measured for the FET device for various gate voltages V_G .

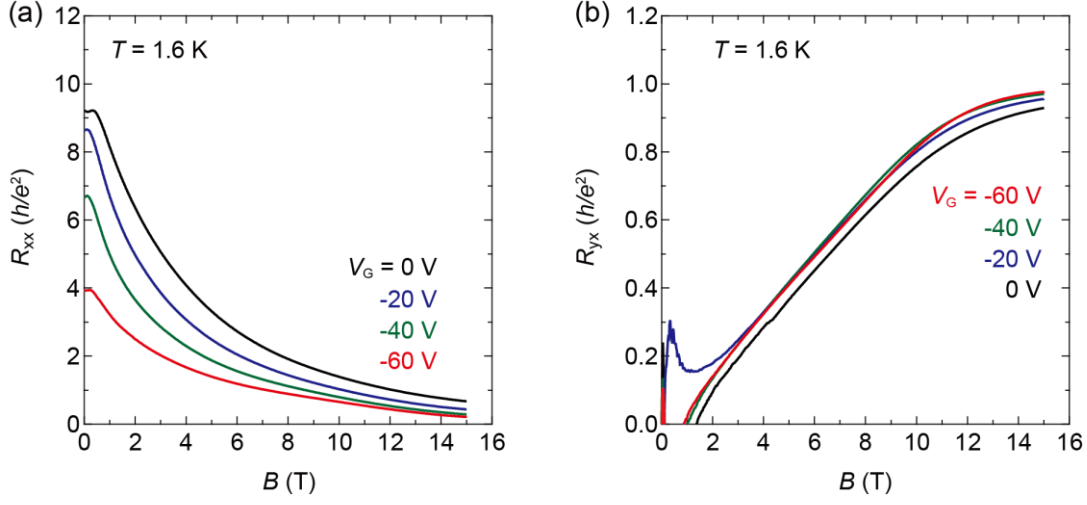


FIG. S7. $R_{xx}(B)$ and $R_{yx}(B)$ of the FET device of the trilayer structure under various V_G .

(a,b) Magnetic-field dependences of (a) R_{xx} and (b) R_{yx} measured for the FET device based on trilayer at $T = 1.6$ K under various V_G .

Figure S7 shows magnetic-field dependence of R_{xx} and R_{yx} for the FET device based on the trilayer (the inset of Fig. 3(b) in the main text) at $T = 1.6$ K under $V_G = 0$ V (black), -20 V (blue), -40 V (green), and -60 V (red). At zero magnetic field, applying a negative V_G decreases R_{xx} . By sweeping B in the negative V_G , longitudinal resistance R_{xx} decreases towards zero and Hall resistance R_{yx} almost reaches quantized resistance h/e^2 .

8. $R_{xx}(T)$ and $R_{yx}(T)$ measured for the FET device under various magnetic fields.

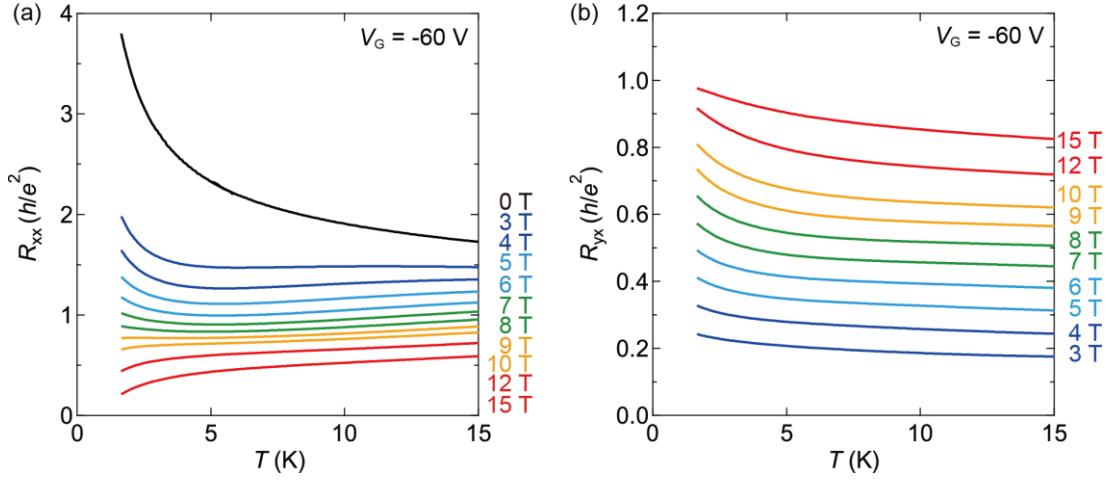


FIG. S8. (a,b) Temperature dependences of (a) R_{xx} and (b) R_{yx} of the FET device of the trilayer structure with $V_G = -60$ V under various B .

Figure S8 shows temperature dependences of R_{xx} and R_{yx} for the FET device based on the trilayer (the inset of Fig. 3(b) in the main text) at $V_G = -60$ V under various perpendicular magnetic field B from 0 T (black) to 15 T (red). At zero magnetic field, $R_{xx}(T)$ shows insulating behavior. By increasing B , longitudinal resistance R_{xx} decreases and becomes metallic and Hall resistance R_{yx} increases and almost reaches quantized resistance h/e^2 under $B = 15$ T at $T = 1.6$ K. At low field, $R_{yx}(T)$ cannot properly measured owing to high longitudinal resistance.

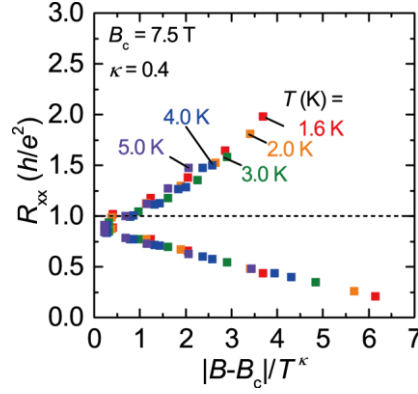


Figure S9 | R_{xx} plotted against the scaled magnetic field $|B - B_c|/T^\kappa$ at different temperature T . The data are extracted from T dependence of R_{xx} measured at different B presented in Fig. S8.

We used the scaling relation that R_{xx} is a function of $|B - B_c|/T^\kappa$ to scale $R_{xx}(T)$ measured at different magnetic field presented in Fig. S8. Figure S9 shows R_{xx} at typical temperatures ($T = 1.6, 2.0, 3.0, 4.0,$ and 5.0 K) are plotted in $|B - B_c|/T^\kappa$ by substituting 7.5 T and 0.4 into the critical magnetic field B_c and the critical exponent κ . The curves at different T converge to a single curve around the critical point. The critical magnetic field $B_c \sim 7.5$ T is consistent with renormalization group flow of the conductivity tensor discussed in main Fig. 4.

9. Estimation of energies accounting for band crossing in Fe-doped (Bi,Sb)₂Se₃/Bi₂Se₃ bilayer.

It is anticipated that the QAH phase can occur if $\Delta_{\text{Zeeman}}^2 > V^2 + \Delta_{\text{hy}}^2$, where V is the energy difference between the positions of the Dirac point at the top and bottom surfaces [18,19]. In addition, the scattering broadening of surface states $\gamma \cong \hbar/\tau$ must be considered. Here, \hbar and τ are the reduced Planck's constant and the electron lifetime, usually shorter than the momentum relaxation time. We estimate that it is below $\gamma \cong 40$ meV. Zeeman energy of $\Delta_{\text{Zeeman}} = g_s \mu_B B$ with g_s and μ_B being effective g -factor and Bohr magneton, is estimated as approximately 16–43 meV in $B = 15$ T when using the reported value of the g -factor $g_s = 18$ –50 for the surface state of Bi₂Se₃ [20,21]. Actually, because of sp - d exchange interactions between band carriers and spins localized on the d shells of magnetic ions, the Zeeman splitting can be enhanced in semiconductors containing transition-metal impurities [22-25]. It is anticipated that similar enhancement of the g -factor in Fe-doped Bi₂Se₃ engenders Δ_{Zeeman} larger than V and γ . As explained below, the value of V is estimated to be 80 meV. The typical value of Δ_{hy} in Bi₂Se₃ thin films is 0.1-0.2 eV [6]. Therefore, the g -factor that requires to fulfil the relation $\Delta_{\text{Zeeman}}^2 > V^2 + \Delta_{\text{hy}}^2$, is roughly 250 under the application of the magnetic field of 15 T.

9-1. Potential variation V at top and bottom surface states

Energy difference between the Dirac points at the top and bottom surfaces corresponds to built-in potential of the p - n junction in the relevant Fe_x(Bi,Sb)₂Se₃/Bi₂Se₃ bilayer structure. From Poisson's equation for the semiconductor p - n junction, built-in potential (V_{bi}) is given as $V_{\text{bi}} = e/\varepsilon_r \varepsilon_0 (nd_n^2 + pd_p^2)$, where e , ε_r , and

e_0 respectively represent the elementary charge, dielectric constant, permittivity of vacuum, and where n , p , d_n , and d_p respectively represent electron and hole carrier densities and the depletion layer thickness in the n and p -type region. V_{bi} in the bilayer system can be calculated as approximately 80 meV using parameters extracted from earlier reports $p = 5 \times 10^{18} \text{ cm}^{-3}$ and $d_p = 12 \text{ nm}$ for $(\text{Bi,Sb})_2\text{Se}_3/\text{Bi}_2\text{Se}_3$ bilayer and $n = 2 \times 10^{19} \text{ cm}^{-3}$ and $d_n = 3 \text{ nm}$ for Bi_2Se_3 [5]. In addition, the dielectric constant of Bi_2Se_3 ($\epsilon_r = 100$) is used for calculations [26].

9-2. Scattering broadening

Scattering broadening γ of electronic states is of the order of $\hbar/\tau = \hbar e/\mu m_c$, where \hbar and τ respectively represent the reduced Planck's constant and electron scattering time, and where e , μ , and m_c represent the elemental charge, electron mobility, and effective mass. Using the measured value of $\mu = 300 \text{ cm}^2\text{V}^{-1}\text{s}^{-1}$ for non-Fe-doped $(\text{Bi,Sb})_2\text{Se}_3/\text{Bi}_2\text{Se}_3$ bilayer [1] and the reported value of $m_c = 0.1 m_0$ [21], γ can be evaluated as approximately 40 meV.

9-3. g -factor enhancement in dilute magnetic semiconductors

A unique feature in dilute magnetic semiconductors is so-called giant Zeeman splitting, which results from $sp-d$ exchange interactions [22,23]. Aligning local magnetic moments of magnetic impurities by an external magnetic field induces large Zeeman splitting in the conduction and valence bands via the $sp-d$ exchange interaction. A typical value of the Zeeman splitting in Mn or Fe-doped II-VI semiconductors

reaches a few tens of milli-electron volts in the presence of a magnetic field of a few Teslas and at low temperatures [24,25].

9-4. Reported values for the gap energy and related values for magnetic (Bi,Sb)₂Te₃

The size of the gap energy of surface states in a ferromagnetic Cr_{0.08}(Bi_{0.1}Sb_{0.9})_{1.92}Te₃ was reported as approximately 30 meV using scanning tunneling microscopy [27]. Scattering broadening γ can be estimated as approximately 25 meV using reported values of $\mu \sim 500 \text{ cm}^2\text{V}^{-1}\text{s}^{-1}$ [9] and $m_c \sim 0.1 m_0$ [28] for (Bi,Sb)₂Te₃.

10. Gate voltage dependence of $R_{xx}(B)$ and $R_{yx}(B)$ in a field-effect transistor (FET)

based on the trilayer structure.

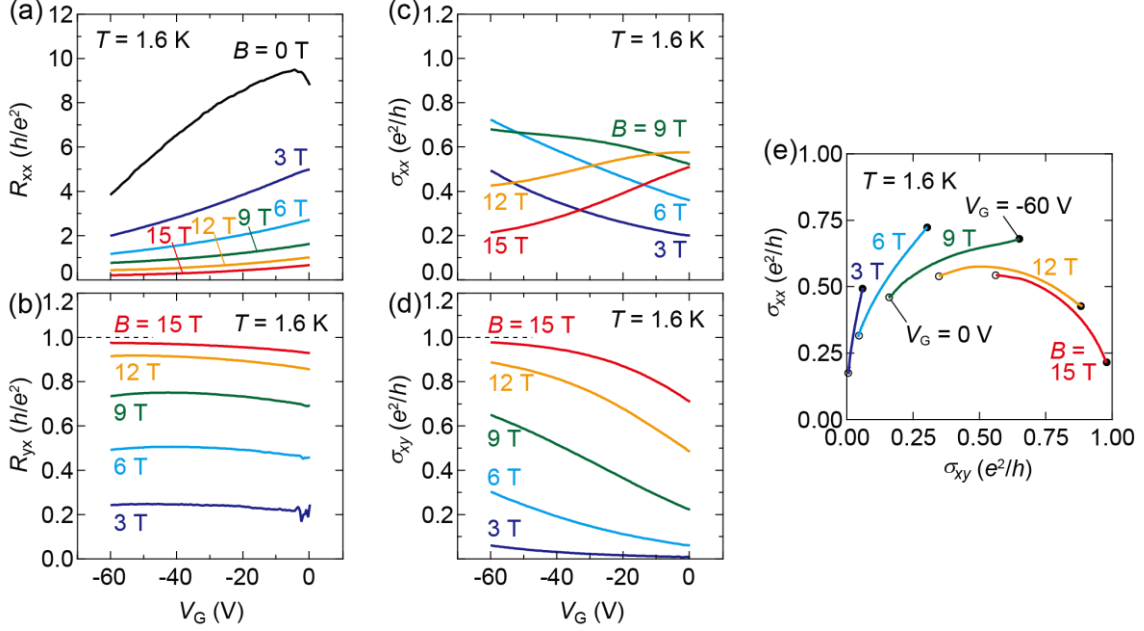


FIG. S10. Dependence of R_{xx} and R_{yx} on the gate voltage V_G at various magnetic fields.

(a-d) V_G dependence of (a) longitudinal resistance R_{xx} ; (b) Hall resistance R_{yx} ; (c) longitudinal conductivity σ_{xx} and (d) Hall conductivity σ_{xy} under various magnetic fields $B = 0$ (black), 3 (blue), 6 (cyan), 9 (green), 12 (orange), and 15 T (solid red line) at $T = 1.6$ K in the field-effect transistor device presented in Figs. 3(b) and 4 in the main text. (e) $\sigma_{xx}(V_G)$, $\sigma_{xy}(V_G)$ plot at $T = 1.6$ K for various magnetic fields. Empty and filled circles represent data at $V_G = 0$ V and -60 V.

Figure S10 presents dependence of R_{xx} and R_{yx} on the gate voltage V_G in the field-effect transistor device consisting of a 1-nm-thick Bi_2Se_3 /18.5-nm-thick $\text{Fe}_{0.05}(\text{Bi}_{0.33}\text{Sb}_{0.67})_{1.95}\text{Se}_3$ /3-nm-thick Bi_2Se_3 tri-layer structure (inset to Fig. 3(b)). Under $B = 15$ T, σ_{xx} and σ_{xy} converge to $(\sigma_{xx}, \sigma_{xy}) = (0, e^2/h)$ of the quantum anomalous phase

by sweeping V_G to the negative value, as shown in Fig. S10(e). The result indicates that the Fermi level approaches the magnetic-field-induced gap at the Dirac point by negative V_G . Moreover, at $B = 9$ and 12 T, the data point of $(\sigma_{xx}, \sigma_{xy})$ moves from the trivial region $\sigma_{xy} < 0.5 e^2/h$ to QAH region by application of V_G . Detailed measurement of temperature dependence is necessary to ascertain the ground state; we leave this assessment as a subject for future study.

11. Structural analysis

Figure S11 presents x-ray diffraction patterns and atomic force microscopic images of 15-nm-thick Fe-doped $(\text{Bi,Sb})_2\text{Se}_3$ layers with Fe content up to $x = 0.2$. For $x = 0$ (bottom panel), a clear diffraction peak (solid triangle) is observed at the 2θ angle of 18.6° , which is assigned to $(\text{Bi,Sb})_2\text{Se}_3$ (0006). At the same time, a step-and-terrace structure is observed using AFM, as reported already [1]. For $x = 0.05$, an identical diffraction pattern and step-and-terrace structure are found. When x is increased to 0.10, rectangular precipitates start to appear on the surface. For $x = 0.20$, the number of such precipitates increases. An additional x-ray diffraction peak appears at around 2θ angle of 16.1° , which we assigned to Fe_3Se_4 (001) [29]. Based on the results of analyses presented above, we evaluate the solubility limit of Fe as approximately $x = 0.1$.

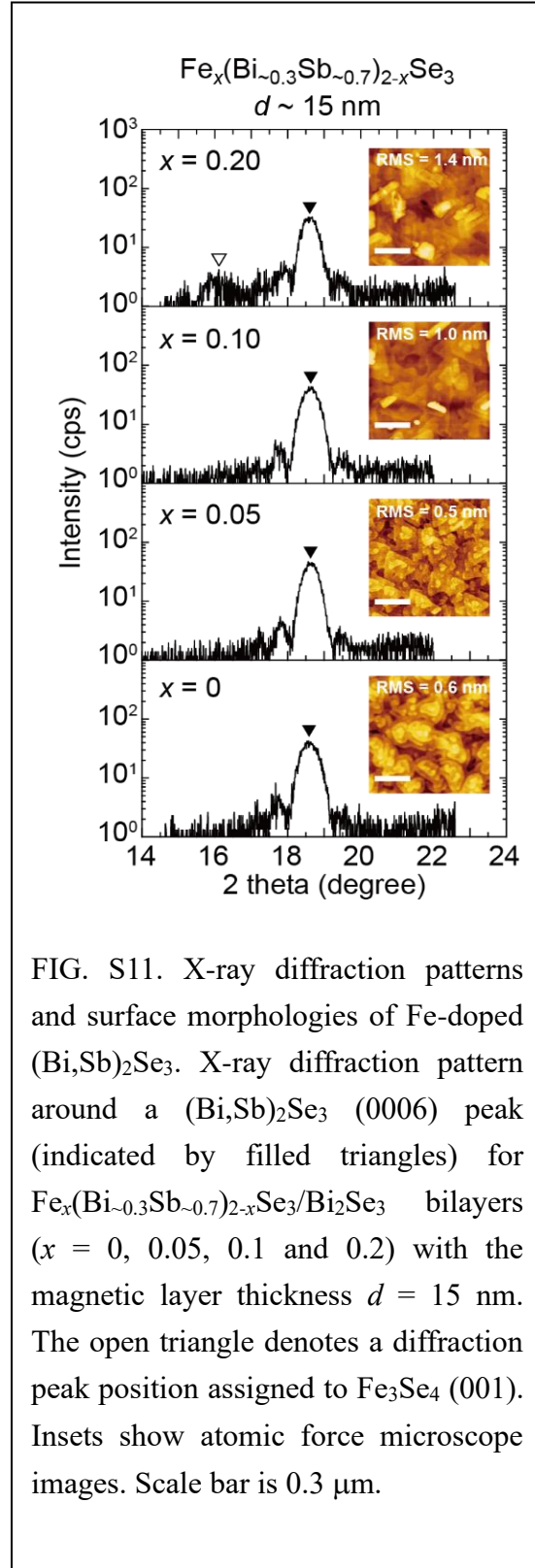


FIG. S11. X-ray diffraction patterns and surface morphologies of Fe-doped $(\text{Bi,Sb})_2\text{Se}_3$. X-ray diffraction pattern around a $(\text{Bi,Sb})_2\text{Se}_3$ (0006) peak (indicated by filled triangles) for $\text{Fe}_x(\text{Bi}_{\sim 0.3}\text{Sb}_{\sim 0.7})_{2-x}\text{Se}_3/\text{Bi}_2\text{Se}_3$ bilayers ($x = 0, 0.05, 0.1$ and 0.2) with the magnetic layer thickness $d = 15 \text{ nm}$. The open triangle denotes a diffraction peak position assigned to Fe_3Se_4 (001). Insets show atomic force microscope images. Scale bar is $0.3 \mu\text{m}$.

Supplementary References

1. Y. Satake, J. Shiogai, D. Takane, K. Yamada, K. Fujiwara, S. Souma, T. Sato, T. Takahashi, and A. Tsukazaki, Fermi-level tuning of the Dirac surface state in $(\text{Bi}_{1-x}\text{Sb}_x)_2\text{Se}_3$ thin films, *J. Phys.: Condens. Matter* **30**, 085501 (2018).
2. C. L. Song, Y. P. Jiang, Y. L. Wang, Z. Li, L. Wang, K. He, X. Chen, X. C. Ma, and Q. K. Xue, Gating the charge state of single Fe dopants in the topological insulator Bi_2Se_3 with a scanning tunneling microscope, *Phys. Rev. B* **86**, 045441 (2012).
3. M. M. Yee, Z. H. Zhu, A. Soumyanarayanan, Y. He, C. L. Song, E. Pomjakushina, Z. Salman, A. Kanigel, K. Segawa, Y. Ando, and J. E. Hoffman, Spin-polarized quantum well states on $\text{Bi}_{2-x}\text{Fe}_x\text{Se}_3$, *Phys. Rev. B* **91**, 161306(R) (2015).
4. S. Awaji, K. Watanabe, H. Oguro, H. Miyazaki, S. Hanai, T. Tosaka, and S. Ioka, First performance test of a 25 T cryogen-free superconducting magnet, *Supercond. Sci. Technol.* **30**, 065001 (2017).
5. Y. Satake, J. Shiogai, K. Fujiwara, and A. Tsukazaki, Effect of the depletion region in topological insulator heterostructures for ambipolar field-effect transistors, *Phys. Rev. B* **98**, 125415 (2018).
6. Y. Zhang, K. He, C. Z. Chang, C. L. Song, L. L. Wang, X. Chen, J. F. Jia, Z. Fang, X. Dai, W. Y. Shan *et al.*, Crossover of the three-dimensional topological insulator Bi_2Se_3 to the two-dimensional limit, *Nat. Phys.* **6**, 584 (2010).

7. Y. Y. Li, G. Wang, X. G. Zhu, M. H. Liu, C. Ye, X. Chen, Y. Y. Wang, K. He, L. Wang, X. C. Ma *et al.*, Intrinsic topological insulator Bi₂Te₃ thin films on Si and their thickness limit, *Adv. Mater.* **22**, 4002 (2010).
8. Y. S. Kim, M. Brahlek, N. Bansal, E. Edrey, G. A. Kapilevich, K. Iida, M. Tanimura, Y. Horibe, S. W. Cheong, and S. Oh, Thickness-dependent bulk properties and weak antilocalization effect in topological insulator Bi₂Se₃, *Phys. Rev. B* **84**, 073109 (2011).
9. Y. Jiang, Y. Wang, M. Chen, Z. Li, C. Song, K. He, L. Wang, X. Chen, X. Ma, and Q. K. Xue, Landau quantization and the thickness limit of topological insulator thin films of Sb₂Te₃, *Phys. Rev. Lett.* **108**, 016401 (2012).
10. A. A. Taskin, S. Sasaki, K. Segawa, and Y. Ando, Manifestation of topological protection in transport properties of epitaxial Bi₂Se₃ thin films, *Phys. Rev. Lett.* **109**, 066803 (2012).
11. G. Landolt, S. Schreyeck, S. V. Eremeev, B. Slomski, S. Muff, J. Osterwalder, E. V. Chulkov, C. Gould, G. Karczewski, K. Brunner *et al.*, Spin texture of Bi₂Se₃ thin films in the quantum tunneling limit, *Phys. Rev. Lett.* **112**, 057601 (2014).
12. J. Zhang, C. Z. Chang, Z. Zhang, J. Wen, X. Feng, K. Li, M. Liu, K. He, L. Wang, X. Chen *et al.*, Band structure engineering in (Bi_{1-x}Sb_x)₂Te₃ ternary topological insulators, *Nat. Commun.* **2**, 574 (2011).
13. M. Brahlek, N. Koirala, M. Salehi, N. Bansal, and S. Oh, Emergence of decoupled surface transport channels in bulk insulating Bi₂Se₃ thin films, *Phys. Rev. Lett.* **113**, 026801 (2014).

14. M. Kawamura, M. Mogi, R. Yoshimi, A. Tsukazaki, Y. Kozuka, K. S. Takahashi, M. Kawasaki, and Y. Tokura, Topological quantum phase transition in magnetic topological insulator upon magnetization rotation, *Phys. Rev. B* **98**, 140404(R) (2018).
15. J. Linder, T. Yokoyama, and A. Sudbø, Anomalous finite size effects on surface states in the topological insulator Bi_2Se_3 , *Phys. Rev. B* **80**, 205401 (2009).
16. J. Zhang, C. Z. Chang, P. Tang, Z. Zhang, X. Feng, K. Li, L. Wang, X. Chen, C. Liu, W. Duan *et al.*, Topology-driven magnetic quantum phase transition in topological insulators, *Science* **339**, 1582 (2013).
17. H. Jin, J. Im, and A. J. Freeman, Topological and magnetic phase transitions in Bi_2Se_3 thin films with magnetic impurities, *Phys. Rev. B* **84**, 134408 (2011).
18. R. Yu, W. Zhang, H. J. Zhang, S. C. Zhang, X. Dai, and Z. Fang, Quantized anomalous Hall effect in magnetic topological insulators, *Science* **329**, 61 (2010).
19. X. Feng, Y. Feng, J. Wang, Y. Ou, Z. Hao, C. Liu, Z. Zhang, L. Zhang, C. Lin, J. Liao *et al.*, Thickness dependence of the quantum anomalous Hall effect in magnetic topological insulator films, *Adv. Mater.* **28**, 6386 (2016).
20. Y. S. Fu, T. Hanaguri, K. Igarashi, M. Kawamura, M. S. Bahramy, and T. Sasagawa, Observation of Zeeman effect in topological surface state with distinct material dependence, *Nat. Commun.* **7**, 10829 (2016).
21. J. G. Analytis, R. D. McDonald, S. C. Riggs, J. H. Chu, G. S. Boebinger, and I. R. Fisher, Two-dimensional surface state in the quantum limit of a topological insulator, *Nat. Phys.* **6**, 960 (2010).

22. P. Kacman, Spin interactions in diluted magnetic semiconductors and magnetic semiconductor structures, *Semicond. Sci. Technol.* **16**, R25 (2001).
23. T. Dietl, (Diluted) magnetic semiconductor, in *Handbook on Semiconductors* (Elsevier, Amsterdam, 1994), Vol **3b**, p. 1251.
24. J. K. Furdyna, Diluted magnetic semiconductors, *J. Appl. Phys.* **64**, R29 (1988).
25. A. Twardowski, K. Pakula, I. Perez, P. Wise, and J. E. Crow, Magnetorefectance and magnetization of the semimagnetic semiconductor $\text{Cd}_{1-x}\text{Fe}_x\text{Se}$, *Phys. Rev. B* **42**, 7567 (1990).
26. D. Kim, S. Cho, N. P. Butch, P. Syers, K. Kirshenbaum, S. Adam, J. Paglione, and M. S. Fuhrer, Surface conduction of topological Dirac electrons in bulk insulating Bi_2Se_3 , *Nat. Phys.* **8**, 459 (2012).
27. I. Lee, C. K. Kim, J. Lee, S. J. L. Billinge, R. Zhong, J. A. Schneeloch, T. Liu, T. Valla, J. M. Tranquada, G. Gu, and J. C. Séamus Davis, Imaging Dirac-mass disorder from magnetic dopant atoms in the ferromagnetic topological insulator $\text{Cr}_x(\text{Bi}_{0.1}\text{Sb}_{0.9})_{2-x}\text{Te}_3$, *Proc. Natl Acad. Sci. USA* **112**, 1316 (2015).
28. R. Akiyama, K. Sumida, S. Ichinokura, R. Nakanishi, A. Kimura, K. A. Kokh, O. E. Tereshchenko, and S. Hasegawa, Shubnikov-de Haas oscillations in p and n -type topological insulator $(\text{Bi}_x\text{Sb}_{1-x})_2\text{Te}_3$, *J. Phys.: Condens. Matter* **30**, 265001 (2018).
29. H. M. N. Vasconcelos, M. Eddrief, Y. Zheng, D. Demaille, S. Hidki, E. Fonda, A. Novikova, J. Fujii, P. Torelli, B. R. Salles *et al.*, Magnetically hard Fe_3Se_4

embedded in Bi₂Se₃ topological insulator thin films grown by molecular beam epitaxy, ACS Nano **10**, 1132 (2016).